metals

MDPI

Review

A Review of Sheet Metal Forming Evaluation of Advanced High-Strength Steels (AHSS)

Rui Pereira [1,2,*], Nuno Peixinho [1,2] and Sérgio L. Costa [3]

[1] Mechanical Engineering Department (DEM), University of Minho, Campus de Azurém Avenida da Universidade, 4800-058 Guimarães, Portugal; peixinho@dem.uminho.pt
[2] Mechanical Engineering and Resource Sustainability Center (MEtRICs), Campus de Azurém Alameda da Universidade, 4800-058 Guimarães, Portugal
[3] Bairrimoldes Lda, Variante à EN 235 n°33, 3780-292 Anadia, Portugal; sergiocosta@bairrimoldes.pt
* Correspondence: id10650@alunos.uminho.pt

Abstract: This paper presents a review on the formability evaluation of AHSS, enhancing necking-based failure criteria limitations. Complementary fracture/damage constitutive modeling approaches specifically tailored to formability evaluation, validated through numerical and experimental methods, are also subjects of research. AHSS are widely processed through sheet metal forming processes. Although an excellent choice when lightweight, high-strength, and ductility are critical factors, their multi-phase microstructure accentuates forming challenges. To accurately model forming behavior, necking-based failure criteria as well as direct fracture models require improvements. As a necking-based failure model, the conventional forming limit diagram/curve (FLD/FLC) presents limitations in estimating direct fracture (surface cracks, edge cracks, shear cracks), as well as deformation histories under non-linear strain paths. Thus, significant research efforts are being made towards the development of advanced fracture constitutive models capable of predicting fracture scenarios without necking, which are more frequently observed in the realm of AHSS. Scientific community research is divided into several directions aiming at improving the forming and fracture behavior accuracy of parts subjected to sheet metal forming operations. In this review paper, a comprehensive overview of ductile fracture modeling is presented. Firstly, the limitations of FLD/FLC in modeling fracture behavior in sheet metal forming operations are studied, followed by recent trends in constitutive material modeling. Afterwards, advancements in material characterization methods to cover a broad range of stress states are discussed. Finally, damage and fracture models predicting failure in AHSS are investigated. This review paper supplies relevant information on the current issues the sheet metal forming community is challenged with due to the trend towards AHSS employment in the automotive industry.

Keywords: AHSS; failure models; FLD/FLC limitations

check for updates

Citation: Pereira, R.; Peixinho, N.; Costa, S.L. A Review of Sheet Metal Forming Evaluation of Advanced High-Strength Steels (AHSS). *Metals* **2024**, *14*, 394. https://doi.org/10.3390/met14040394

Academic Editors: Haijiang Hu and Junyu Tian

Received: 19 February 2024
Revised: 25 March 2024
Accepted: 26 March 2024
Published: 28 March 2024

Copyright: © 2024 by the authors. Licensee MDPI, Basel, Switzerland. This article is an open access article distributed under the terms and conditions of the Creative Commons Attribution (CC BY) license (https://creativecommons.org/licenses/by/4.0/).

1. Introduction

The 2023 European Union (EU) environment report highlights the transportation sector's 25% share of greenhouse gas emissions [1]. The EU aims for a 23% transport emission reduction by 2030 compared to 2005 levels. In vehicles, a 10% weight reduction corresponds to a fuel consumption saving of 6.5% [2]. Automobile manufactures prioritize lightweight construction to reduce CO_2 emissions and fossil fuel use in vehicles [3–5]. New car emissions have decreased notably, with 12% declines for both 2020 and 2021. This trend is partially attributed to the reduction of Body in White (BiW) components' overall weight, which are the main contributors to the overall weight of vehicles [6]. Along with environmental concerns, passenger safety may never be compromised. In order to comprise lightweight construction, safety, and structural performance, vehicle material list have been continuously shifting through the employment of a higher variety of materials,

e.g., through the usage of aluminum alloys and Advanced High-Strength Steels (AHSS). Trzepiecinski and Najm provide a comprehensive overview of the applications of metallic materials in the automotive industry [7].

The use of AHSS have become increasingly popular in the automotive industry due to their appropriate mechanical properties, namely, high structural strength, high stiffness, high work hardening capacity, low cost, high performance, and mass optimization capacity [8], while maintaining good levels of ductility [9,10]. Figure 1 presents the relationship between Ultimate Tensile Strength (UTS) and Total Elongation of AHSS compared to conventional steels. As observed, the greater tensile strength of AHSS grades renders them as a preferable alternative to conventional mild steels, as thinner sheets can be used. Similarly, the enhanced high-strength-to-density ratio of AHSS materials makes them a strong competitor of aluminum and magnesium alloys.

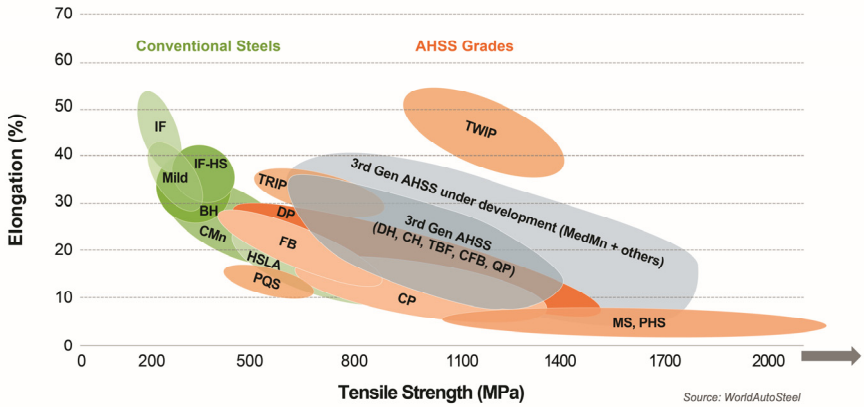

Figure 1. Banana chart of steels used in automotive applications: UTS vs. Total Elongation [11]. Courtesy of WorldAutoSteel [12].

Sheet metal forming operations are widely employed in the automotive second tier [13,14]. Table 1 summarizes AHSS types, characteristics, and common applications in the automotive industry. The manufacturing of Body in White components heavily relies on various sheet metal forming processes, such as stamping and deep drawing. Although the major advantages of AHSS employment, the forming process of such materials is increasingly complex. This can be attributed to their multiphase microstructural composition, high yield strength, as well as the thinner sheet thickness considered. Thus, the usage of AHSS intensifies and introduces forming challenges almost never encountered before. These forming challenges are depicted in Figure 2. The significant yield strength leads to higher forming forces, energy consumption, and higher stresses [15,16], thus requiring the selection of appropriate press machines. Moreover, AHSS exhibit a greater tendency to wrinkle due to the lack of adequate hold-down, and a reduction of sheet thickness is frequently observed. Springback and dimensional control inconsistencies are accentuated, requiring the need for tooling shape modification and/or adoption of progressive die compensation techniques [17–20]. On the other hand, the multi-phase microstructure of AHSS leads to batch-to-batch inconsistencies. Simultaneously, die designs are getting increasingly complex. Sharp edges and quick curvature changes are frequently introduced to meet aesthetic concerns [21].

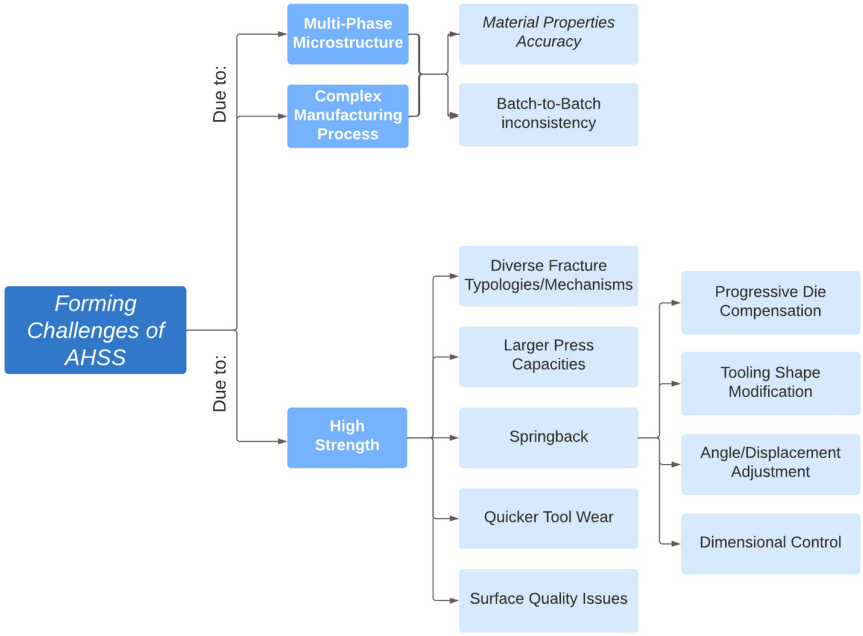

Figure 2. Forming challenges of AHSS. Adapted from [4,16,22].

In accordance with the aforementioned forming challenges associated with manufacturing AHSS, the evaluation of the sheet metal forming process solely through the analysis of the traditional forming limit diagrams (FLDs) can lead to inadequate and misleading interpretations. The material susceptibility to different fracture typologies increases with the employment of AHSS, thereby justifying the need for more accurate fracture modeling of sheet metal forming operations [23]. Once the factors affecting failure are understood, engineers can minimize the risk of failure. This, in turn, can improve product quality and efficiency, reduce scrap rates, and the number of experimental tryouts [24].

This review paper introduces an assessment of the applicability of the Forming Limit Diagram (FLD) in the post-processing of Advanced High-Strength Steel (AHSS) forming processes. Following this introduction, the limitations of the FLD are discussed. The subsequent discourse emphasizes the critical necessity for advanced and precise fracture/damage models within the realm of AHSS forming processes, thereby accentuating their significance in the contemporary analysis of post-processing results for AHSS.

Table 1. Summary of different types of 1st generation AHSS: microstructure, mechanical properties, and typical applications. Adapted from [4,7,8,15,25–29].

AHSS	Microstructure	Mechanical Properties				Characteristics	Typical Applications
		$R_{P0.2}$ (MPa)	R_m (MPa)	A80 %	t (mm)		
Dual Phase (**DP**)	Ferrite + Martensite	**DP400**				Conventional: Lower Yield Strength Low Yield-to-Tensile Strength Ratios High Initial Work Hardening No Yield Point Elongation Significant Bake Hardening Good Uniform Elongation High Energy Absorption Good Cold Formability Higher Yield Strength Grades: High Yield-to-Tensile Strength Ratios Some Yield Point Elongation Lower Bake Hardening Reasonable Uniform Elongation Good Energy Absorption	Body Panels; Front and Rear Longitudinal Rails; Supporting Structure Passenger Safety Cages' Components (limited by axial or transverse Bending): Rockers, B-Pillars, Pillar Reinforcements, Roof Rails
		260–340	450–530	27	0.5–2.1		
		DP500					
		290–380	490–600	24	0.5–2.1		
		DP600					
		330–430	590–700	20	0.5–2.1		
		DP800					
		440–550	780–900	14	0.5–2.1		
		DP1000					
		590–900	980–1130	8	0.5–2.1		

Table 1. *Cont.*

AHSS	Microstructure	Mechanical Properties				Characteristics	Typical Applications
		$R_{P0.2}$ (MPa)	R_m (MPa)	A80 %	t (mm)		
Transformation Induced Plasticity (**TRIP**)	Ferrite Matrix + Retained Austenite Hard phase of Bainite and/or Martensite	**TRIP700**				Excellent Combination of Strength and Ductility High Total Elongation Considerable Strain Hardening Capacity High Energy Absorption Excellent Formability High Fatigue Endurance Resistance	Rail Reinforcements; Frame Rails; Crash Box; Side, Roof, Front and Rear Rails; B-Pillar Upper; Seat Frame; Bumper Cross-Members; B-Pillar Reinforcements
		400–520	690–800	24	1		
		TRIP800					
		450–570	780–910	21	1		
Martensitic Steel (**MS**)	Martensitic Matrix + Small Amounts of Ferrite and/or Bainite	**MS900**				High Yield Strength High Tensile Strength Good Hardness High Toughness	Front and Rear Bumpers; Roof Cross Members; Door Beams; EV Battery Protection; Cross Members; Bumper Reinforcements; Bumper Beams; Side Intrusion Beams
		700–1000	900–1100	3	0.5–2.1		
		MS1100					
		860–1100	1100–1300	3	0.5–2.0		
		MS1200					
		950–1200	1200–1400	3	0.5–2.0		
		MS1300					
		1030–1330	1300–1550	3	0.5–2.0		
		MS1500					
		1220–1520	1500–1750	3	0.5–2.1		
		MS1700					
		1350–1700	1700–2000	3	1–2.1		
Complex Phase Steel (**CP**)	Ferrite/Bainite Matrix + Small Amounts of Martensite; Retained Austenite and Pearlite	**CP600**				High Yield Strength Very High Ultimate Tensile Strength Excellent Uniform Ductility High Energy Absorption Excellent True Fracture Strain High Fatigue Strength Good Impact Strength High Residual Deformation Capacity Good Bendability	Seat Flange; Door Bar; Tunnel Stiffeners; Pillar Reinforcements; Bumper and Side Beams; Frame Rails; Rocker Panels; Rear Suspension Brackets; Fender Beams; Seat Tracks
		350–500	600–740	16	0.7–2.5		
		CP800					
		780–950	980–1140	6	0.5–2.1		
		CP1200					
		900–1100	1180–1350	5	0.5–2.1		

2. Failure, Damage, and Fracture in Sheet Metal Forming

Failure and fracture are two distinct terms that are often used interchangeably, although they have different meanings. In the realm of the sheet metal forming community, distinguishing these two terms is particularly important. Failure refers to the point at which the material can no longer withstand the applied stress and loses its ability to maintain its shape due to the loss of load-carrying capacity [30]. Thickness instability is typically referred to as failure. Fracture, on the other hand, relates to the point at which material separation occurs due to excessive stress. Damage is defined as an intermediate state, a product property that accumulates between processes. It represents the undesired evolution of one or more structural characteristics, e.g., micro voids, that hinder an engineering capability [31].

Formability is defined as the ability of sheet metal to be formed into the desired shape without necking or cracking [32]. Thus, formability evaluation should comprise failure mechanisms on account of localized necking and fracture mechanisms not preceded by necking. The FLD criteria lie under the assumption that localized necking precedes damage growth and fracture. In this context, necking instability defines the process limits [23].

From an industrial perspective, the FLD is sufficiently accurate to evaluate components' forming behavior of fracture scenario 1, illustrated in Figure 3. Once localized necking occurs, the component is rejected. However, for scenarios comprising damage growth not preceded by necking instability (scenario 2 and 3), as the FLD does not capture those occurrences, a constitutive fracture/damage model requires implementation to accurately assess components' formability. Fracture scenarios 2 and 3 are more frequently observed in the realm of AHSS. Such eventualities can arise under specific stress states such as

in-plane shear deformation and nearly pure bending loading [21]. Section 4 provides a more in-depth analysis.

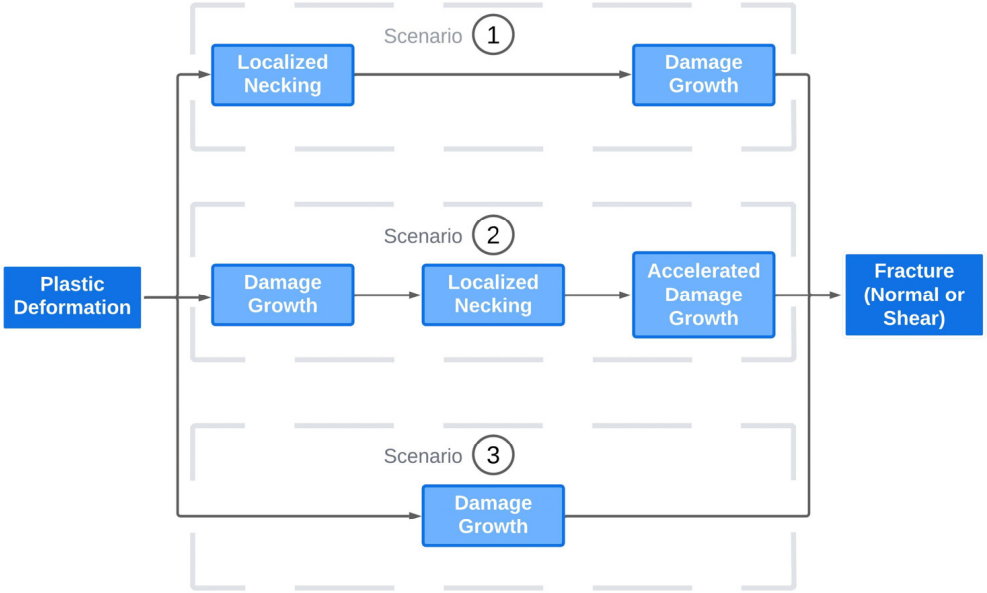

Figure 3. The three fracture scenarios. Adapted from [33].

3. Traditional Forming Limit Diagram (FLD)

Formability evaluation is usually performed through the FLD. The simplicity of representing the principal strains, ε_1 and ε_2, in a graphical way is of great interest for industry. The critical feature of the FLD is the FLC, which describes the strain limits at the onset of necking: the strains located above the FLC fail in a critical state, where necking instability has occurred; the strains behind the FLC are in a safe region, characterized by remaining formability. Therefore, the failure locus for necking instability under various loading conditions, ranging from uniaxial tension to biaxial tension, is depicted by the FLC.

The FLC is affected by different factors. Even for the same material grade, variations in the FLC can be noticed. The reason for that lies in the dependency of factors such as forming temperature [34], material thickness [35], forming speed [35], strain rate [34], friction conditions [36], and strain hardening exponent [37,38]. Liu et al. [39] investigated the strain rate effect through a comparison between AHSS and three different kinds of conventional steels. They concluded that the AHSS are much more dependent on strain rate variations rather than the conventional steels.

3.1. FLC Experimental Determination

The FLC is determined in accordance with the ISO 12004-2_2008 standard [40] using either Nakazima [41] or Marciniak [42] test procedures.

The Nakazima testing method involves the use of specimens with varying cutout widths, which are clamped using a circular blank-holder. Subsequently, the specimens are drawn until fracture through a drawing die by the rectilinear movement of a hemispherical punch. Draw beads in tools are used to restrain the blank between the die and blank-holder and also to avoid stress concentration at the transition from strip section to the blank [43]. Nakazima tests should be executed in frictionless conditions between the contact zone of the punch and specimen pair [44]. As an out-of-plane stretching method, the Nakazima test is dependent on the tool geometries, through-thickness pressure, and lubrification conditions [23]. Most often, Nakazima tests are selected to draw the FLC [45–50].

On the other hand, the Marciniak in-plane test involves the deformation of specimens under balanced biaxial conditions. By modifying the washer and specimen geometries, the FLC can be generated [23]. An adapted design of the punch geometry is adopted in order to minimize the friction in the specimen central region.

Irrespective of the performed method, a wide range of deformation modes can be achieved by modifying the specimen geometry. Figure 4 portrays the influence of specimen geometry on deformation modes. To cover a broad range of deformation modes, at least five different specimen widths must be tested [40]. The FLC's shape is strongly dependent on the strain path and hence on the specimen geometry. The more the specimens are tested, the more accurate the prediction of FLC formability.

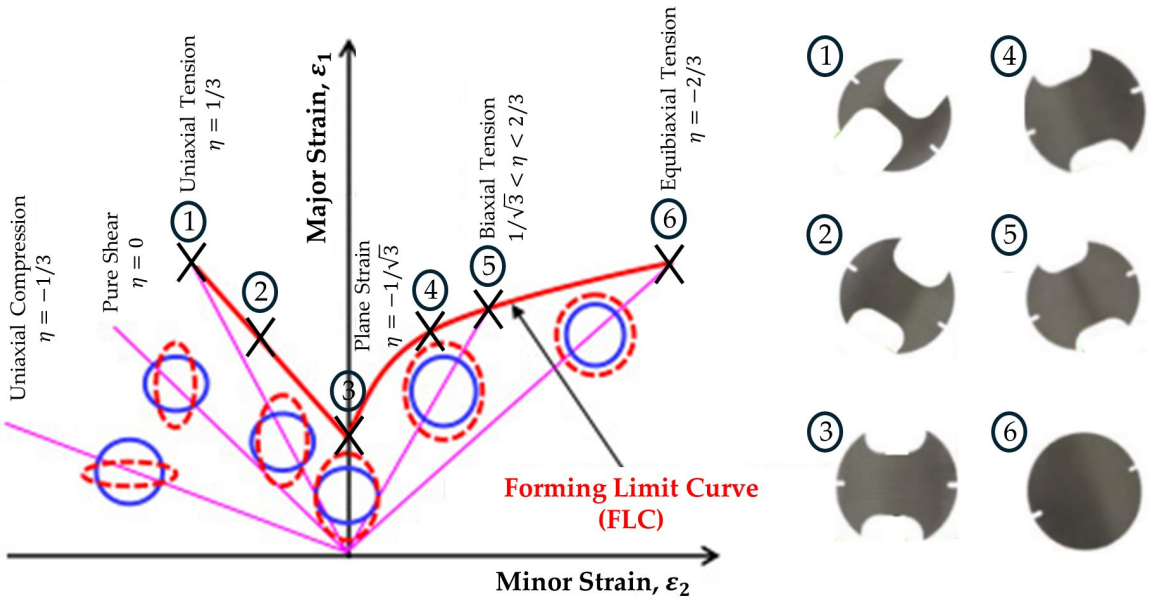

Figure 4. Schematic illustration of FLC in relation to specimen geometries. Adapted from [51,52].

The experimental methods to determine the FLC are usually time-consuming, low cost-effective, and limited by experimental conditions, even though they are more trustable than other approaches [53]. Many researchers select the Nakazima test procedure due to the simplicity of tools required [54].

3.2. Limit Strains' Determination Methods

The accurate assessment of the limit strains is a major step for the experimental determination of the FLC. The onset of localized necking is an instantaneous moment, difficult to detect, and, even more, to measure. Frequently, the limit strain methods' calculations are divided into: (i) position-dependent methods; (ii) time-dependent methods; (iii) time-position-dependent methods.

The position-dependent methods are characterized by the individual, well-established single and unique evaluation of the onset of necking. ISO 12004-2:2008 [40] recommends a position-dependent approach. As a standard, it is intended to provide practices and unify test condition procedures in order to gather consensus between different laboratories. According to this method, the strain variations are analyzed prior to the occurrence of a crack. The procedure for limit strains' determination in accordance with the ISO standard are provided by Martínez-Donaire et al. [55]. An alternative position-dependent method was proposed by Zhang et al. [56] to provide a more stable and precise FLC determination.

The time-dependent methods rely on the analysis of strain, strain rate, or strain acceleration to determine the onset of through-thickness necking. In the work developed by Merklein et al. [57], necking initiation occurs at the highest value of a linear regression coefficient curve, selected based on the rate of change of strain rate. Iquilio et al. [58] developed a more realistic method to precisely calculate the limit strains of stainless steel with a heterogeneous strain distribution. Other time-dependent methods were proposed by Huang and Shi [59], Volk and Hora [60], and Hotz et al. [61]. Overall, these techniques rely on mathematical manipulation of strain rate rather than physical behavior of materials, which can be unreliable due to noise in data signals and may not be applied to all sheet metals [62].

Time-position-dependent methods are hybrid approaches that consider either the temporal evolution of strain, position, or displacement of points on a line drawn perpendicular to the fracture direction [62]. Martínez-Donaire et al. [63] inferred the initiation of necking when the slope in the first special derivative of the vertical displacement remained constant within the necking region. Furthermore, Min et al. [62] established a time–position-dependent method to identify the onset of localized necking under in-plane deformation based on the measured surface geometry of the test specimen.

Although a wide number of limit strain methods are available, there is no consensus about the method to be chosen, since each method possesses its specific applications. Therefore, a continuous search for more accurate, innovative methods to incorporate specific loading conditions and types of fracture is ongoing to handle ISO standard limitations, namely: (i) unfit for significant strain gradients across the sheet thickness, e.g., when using small punch radii or corner radii in forming dies; (ii) unsuitable in stretch–bending operations; (iii) inapt in multiple necking, implying variable strain distribution; (iv) inappropriate for sudden fracture leading to imprecisions in limit strain, particularly under plane strain or biaxial testing conditions.

3.3. Grid Marking and Deformation Determination Methods

Materials employed in sheet metal forming operations have reduced sheet thickness, particularly the AHSS, where the sheet thickness commonly used is less than 1.5 mm. As a result, surface strain sensitivity significantly increases and requires more advanced strain measurement methods for accurate formability evaluation. FLC determination is influenced by the strain measurement technique employed, implying concerns regarding grid marking type and method, which also plays a key role in addressing major and minor strain calculations. Grid marking is performed prior to the formability test experiment and followed by strain measurement. Figure 5 displays the main tasks involved in FLC determination.

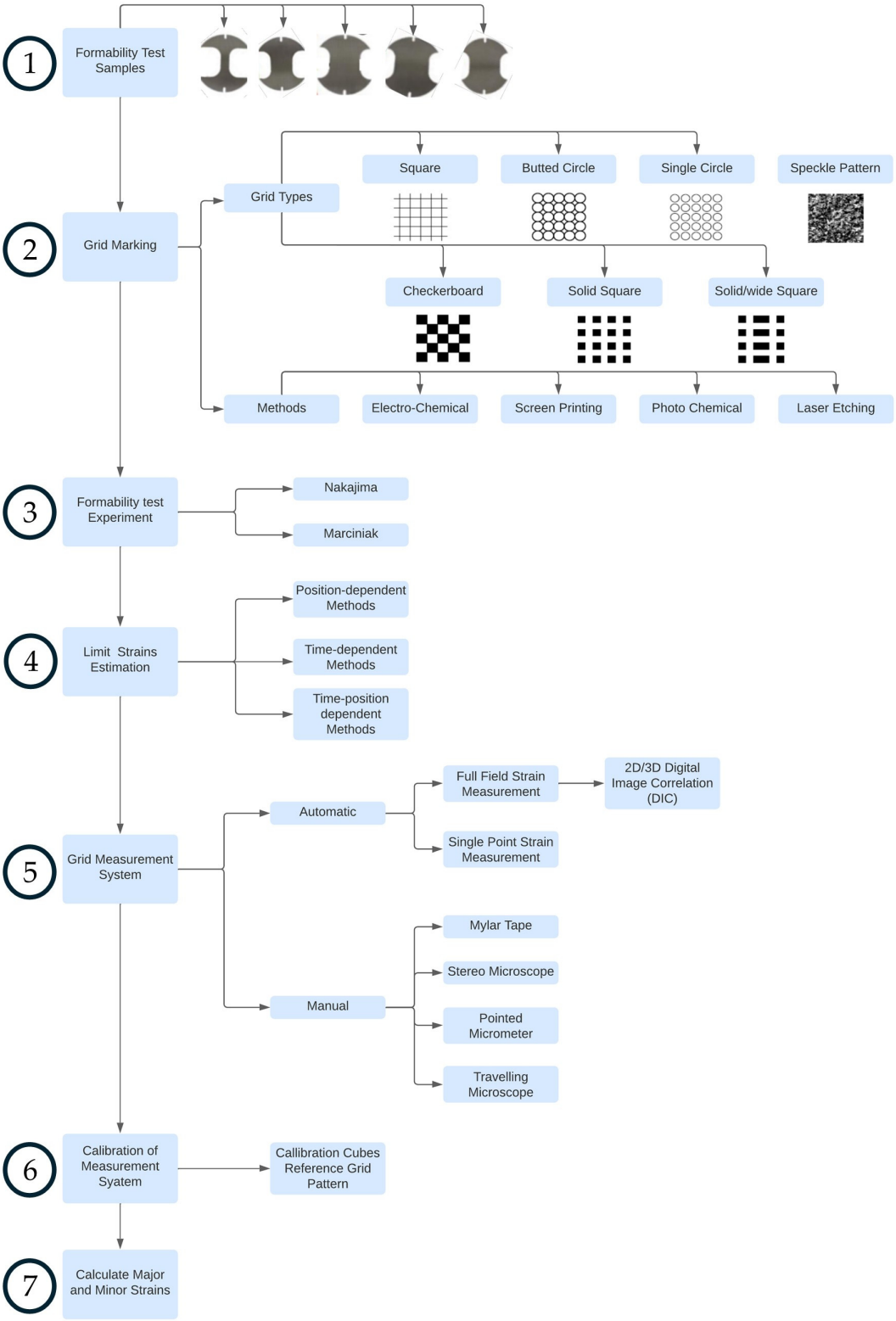

Figure 5. Schematic procedure of the main steps to produce a FLC. Adapted from [53,64].

Grid marking is defined as the process of printing line patterns on the surface of the area of interest on the sheet sample [64]. There are mainly four grid methods for creating grid patterns. Circular or square grid types are the most commonly used for assessing formability. The choice between the available methods must take into consideration parameters such as durability, quality, resolution, contrast, pattern accuracy, and cost.

Nevertheless, one must guarantee the independence of process and forming conditions, such as lubrification and friction, from grid marking [64]. Ozturk et al. [64] introduced the main differences between the overall grid marking methods, and a qualitative comparison of the grid marking methods was appointed. The laser etching process requires the study of power speed, focus, and width parameters [65]. Guk et al. [66] utilized a diode laser marking system to generate grid patterns on multiphase steels; the scanning speed and laser power influence on the mark depth were investigated. Furthermore, Yildiz and Yilmaz [67], after applying four different grid marking methods, namely serigraphy, electro-chemical etching, photo-chemical etching, and laser, concluded that laser is best-suited due to ease of application and stability.

The circular or square patterns are printed before deformation and transform into ellipses or quadrilaterals after the forming operation, respectively. The major and minor strains are determined by comparing previous and subsequent patterns dimensions [68]. ISO 12004-2:2008 [40] stipulates that the dimensions of the grids are related to the thickness of the material, e.g., the circle diameter on circular patterns has a significant impact on strain calculation [69]. Speckle patterns are required to be used simultaneously with Digital Image Correlation (DIC) systems for strain measurement. Li et al. [70] sprayed speckle pattern on the top surface of the sample, and one must guarantee the adhesion of the paint to the surface before and after deformation.

The most practical method of measuring the strains in a formed part is to utilize a measuring grid pattern on the part surface. This can be done either manually or by the use of an automatic method [65]. Manual techniques are characterized by several drawbacks such as high measurement time requirements, less accuracy, and low resolution. However, Bandyopadhyayet et al. [71] adopted a manual strain measurement method to build the stress-based forming limit diagram of a tailor-welded blank material. Additionally, the deformed grids of an Inconel 718 was assessed by means of a stereo microscope [72].

The alternative automatic methods are the Single Point Strain Measurement as well as the Full Field Strain Measurement [53]. Both techniques require less time and have better resolution, hence contributing to more reliable results. The main components in the automatic strain measurement system are the image acquisition hardware and image processing software [73]. ASTM E2218-02 standard [74] provides guidelines for strain measurement.

Single Point Strain Measurement is characterized by the measurement of one grid element separately. Grid Pattern Analyser (GPA) and Forming Measurement Tool Innovations (FMTIs) (http://www.fmtisystems.com/software.htm accessed date: 10 January 2024) are two available commercial software for automatic single-point strain analysis built on image processing. The image acquisition demands machine vision cameras to capture the deformed grids after forming and specialized lenses. Afterwards, the software fits the ellipse to the deformed grids and calculates major and minor principal strains [69].

Full Field Strain Measurement methods, such as Digital Image Correlation (DIC), possess the advantage of measuring larger areas considerably quicker. This method, applicable either in two or three dimensions, require a significant amount of material images prior and after the forming operation with a geometrical relationship between them to derive gradients and correlate them in order to calculate the major and minor strains [75]. As previously mentioned, the DIC system must be used in association with image processing software. The commonly used are namely: German Argus or ARAMIS system of GOM company, the American Grid Analyser Model 100U of the FMTI system Inc. (Hamilton, ON, Canada), the VIC-2D(3D) from the Correlated Solutions Inc. (Irmo, SC, USA), the Dante Dynamics as well as the ICASOF [69,73]. In spite of the high measurement accuracy provided by these systems, they are characterized by an expensive cost [76]. Open source DIC alternatives are a cost-effective solution such as: Ncorr [77], ALDIC [78], py2DIC [79], μDIC [80], and Multi-DIC [81]. Commonly, these alternatives require a huge memory of images taken from a high-speed image acquisition system [69]. The DIC Full Field Strain Measurement Systems have been broadly used to build the FLC [82,83]. Min et al. [84] and Huang and Shi [59] compared standard, spatial, and temporal methods

to determine the onset of localized necking by the use of DIC data. The introduction of these systems, capable of recording and memorizing the whole forming process, has shifted research attention towards time-dependent methods as alternatives to position-dependent methods.

Additionally, DIC may be used to calibrate ductile damage models, evaluate anisotropic materials, as well as to obtain strain distribution either in tensile tests or forming operations. In the work conducted by Gkolfinopoulos and Chijiwa [85], DIC analysis alongside GOM Correlate Professional V8 SR1 commercial software and a full-frame CMOS camera enabled the investigation of strain concentration in the tensile specimen necking region before fracture. The damage model parameters were numerically validated with the aid of DIC analyses.

4. Limitations of FLD

Forming limit diagrams play a crucial role in assessing the formability of metal sheets by defining the maximum strain to failure in terms of major and minor strains. The primary objective is to identify the onset of necking in limited regions of the examined sheet metals [86]. Industrial sheet metal forming manufacturers are interested in the phenomenological outcome observed; as such, the FLD is well-established as a failure criterion. Forming quality evaluation is commonly addressed through FLD in industrial practices, in combination with other indices, such as average springack and thinning rate, which are also used to assess forming response [87]. However, FLD has some limitations with respect to forming behavior modeling accuracy. These limitations are depicted in Figure 6.

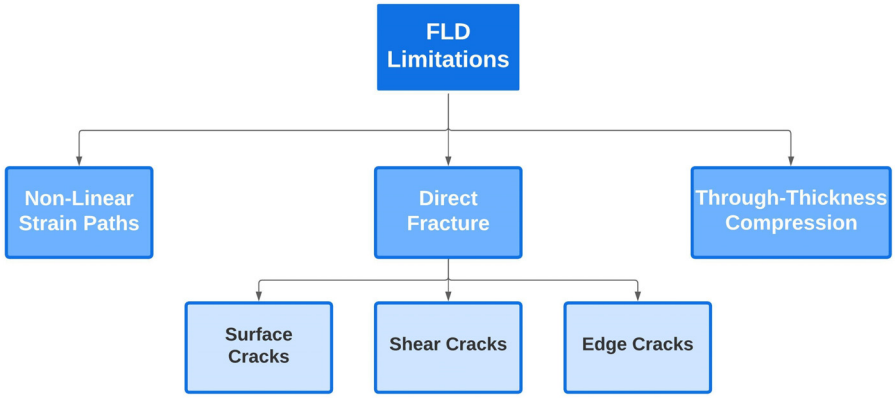

Figure 6. Forming limit diagram limitations.

On one hand, the FLD, as a necking-based failure criterion, is intended to detect through-thickness necks and splits, which lead to a global loss of carrying capacity of the material. Moreover, the range of study of the traditional FLD is limited to the deformation paths illustrated previously in Figure 4. Therefore, the points below the left diagonal are not covered. On the other hand, local instabilities as well as direct fracture on the material's surface are not covered by the FLD analysis. The forming industry's trend towards high strength/low density, alongside sharp geometrical features, accentuates forming challenges. Thus, the need for more advanced models capable of model forming behavior, failure, and fracture is a current demand. AHSS tend to exacerbate these forming challenges in comparison to conventional mild steels; as such, direct fracture on the material's surface is more likely to occur.

To overcome FLD limitations, the special characteristics of AHSS must be taken into consideration. In accordance, more advanced fracture and damage models have been developed to meet the special characteristics of these kinds of materials. Usually, these models require experimental characterization at different stress states [88]. Different specimen geometries and loading conditions are adopted. Section 6 presents the state-of-

the-art testing methods employed for full material characterization. Section 7 addresses the current trends in failure and damage models.

4.1. Non-Linear Strain Paths

The main disadvantage of the traditional FLD is that the different experimental points in the standard FLC are all determined under the assumption of simple proportional loading states. Therefore, it fails to provide proper results for non-linear strain path histories in sheet metal forming processes [89]. In multi-stage forming processes, or even in deep drawing operations under complex loading conditions, the probability of loading paths deviation from linearity is more commonly observed [90]. Furthermore, the traditional LD can also fail to provide adequate precision of the forming process because the material exhibits different strain hardening behavior when a strain path change occurs compared to monotonic loading [91]. Figure 7a illustrates some possible non-linear strain paths observed in sheet metal forming operations. Da Rocha and Jalinier [92] stated that a biaxial solicitation preceded by uniaxial loading leads to increased formability, as opposed to biaxial solicitation followed by uniaxial loading, as illustrated by Figure 7b. Thus, disregarding this shift in loading may result in both conservative and optimistic outcomes with respect to the traditional FLD. Figure 7c presents a deformation path exhibiting high non-linearity leading to failure before the forming limit is reached under the standard FLC.

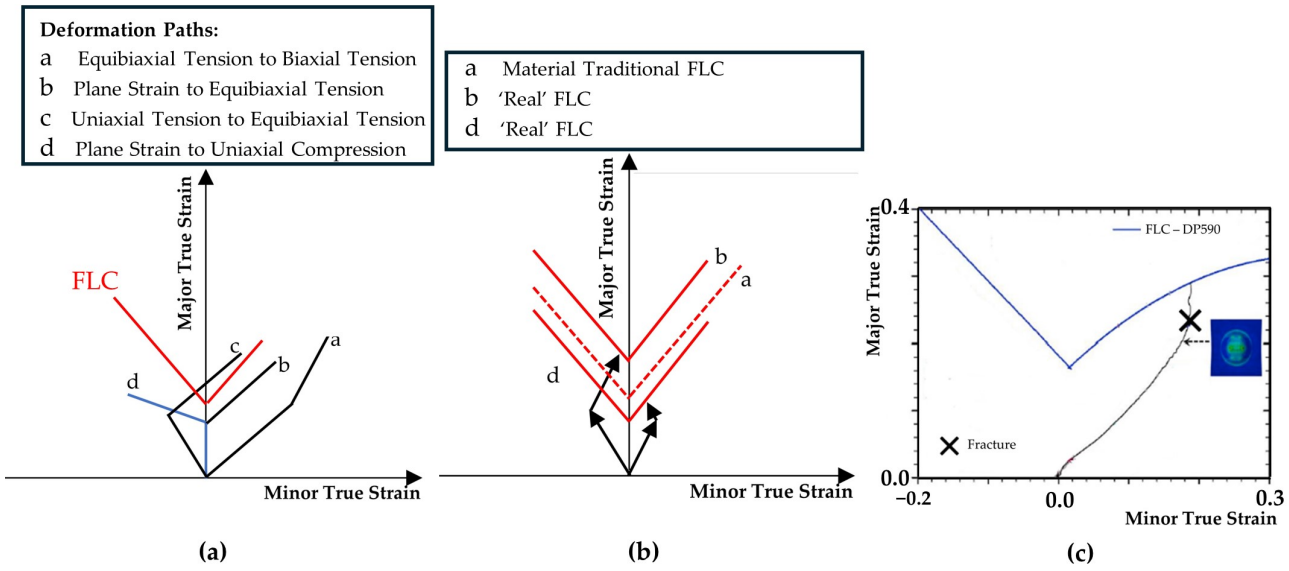

Figure 7. (**a**) Non-linear strain paths; (**b**) non-linearity influence on forming limits; (**c**) non-linear strain path during formation of a component by Fukui stretch drawing test and FLC of DP590 (adapted from [93]).

Manopulo et al. [94] used a theoretical approach based on an extended Modified Maximum Force (eMMF) criterion to account for non-proportional loading. Stress-based models are effective in modeling fracture occurrences in multi-forming operations that are characterized by non-linear strain paths [93]. However, these models may be limited to deformation histories within the Nakazima range. Non-linearities that arise from prede-formation in shear or compression can be effectively modeled by damage accumulation models [21]. Furthermore, the Generalized Forming Limit Curve (GFLC) offers advantages such as its independence from the material model and its ability to represent multilinear strain paths. The GLFC was developed by Volk et al. [95], and it is currently implemented in AutoForm R10. Section 6.2 presents experimental techniques specially designed to address non-linear strain path generation.

4.2. 3D Stress States

Typically, the process of thin sheet forming operates under the plane stress mode [96]. Under this context, the FLD neglects stress in the thickness direction of the sheet. Wang and Wang's [37] research concluded that an FLD that considers induced stress in the thickness direction is more accurate than the FLD of the plane stress mode. In fact, through-thickness shear stresses can improve the forming limit of sheet metals [97]. Moreover, when strain states occur below and within the left diagonal ($\varepsilon_1 = \varepsilon_2$), the presence of a compressive hydrostatic stress component in the thickness direction mitigates the risk of necking. Thus, even under severe thinning, necking will not occur, and the material will deform until the fracture limit is reached. For an accurate prediction of the forming behavior in ironing and coining operations, in-plane shear deformation modes as well as surface defects, the consideration of 3D stress states under the left diagonal of the FLD diagram is required.

The strain increments generated in this region can be analyzed by means of stress triaxiality. Stress triaxiality is a reliable indicator to determine whether a material is subjected to volumetric tension or a compressive stress state. Hence, failure models considering stress triaxiality have garnered attention, as they can identify strain increments arising from a compressive stress state, thereby not contributing to the risk of necking.

4.3. Shear Fracture

Within the realm of AHSS, there is a heightened frequency of shear fracture occurrence on tight radii [98–100]. Shear deformation inherently maintains the thickness of the sheet [21], and the FLD fails to encompass the second quadrant beyond pure shear conditions [101]. The fracture limit in the low triaxiality regime exhibits greater sensitivity to the Lode angle [21]. In fact, the pure shear fracture limit can be significantly lower than the ductile fracture limit [102]. Li et al. [101] have effectively showcased the limitations of the FLD in accurately predicting shear fracture, particularly due to the relatively lower pure shear fracture limit when compared to the uniaxial tension limit, as depicted in Figure 8.

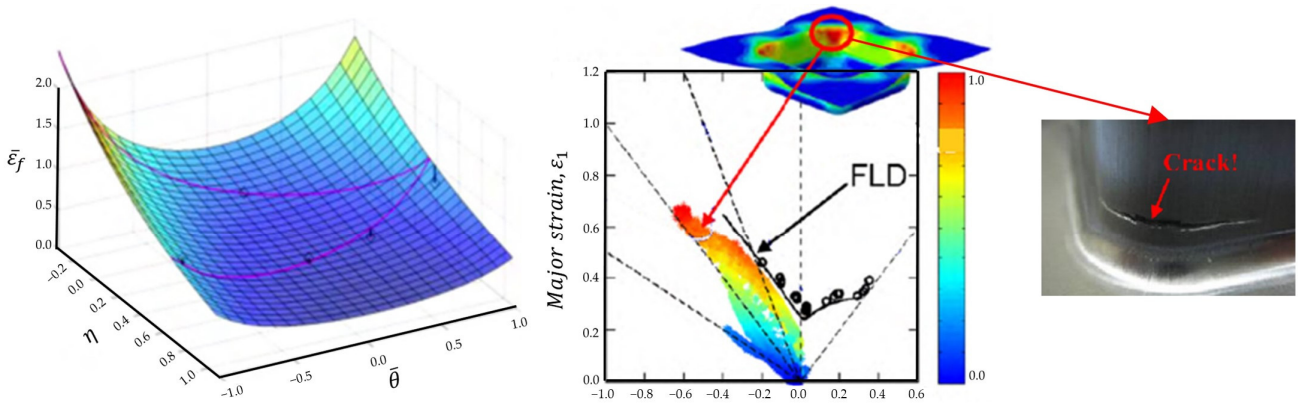

Figure 8. (**a**) 3D fracture locus in the space of equivalent strain to fracture, stress triaxiality, and Lode angle parameter; (**b**) FLD and fracture mode localization. Reprinted from Ref. [101] with permission. Copyright 2010, Elsevier.

The determination of fracture limits in pure in-plane shear remains an area of ongoing investigation, as there is currently no established standardized experimental method for characterizing shear fracture modes. The main difficulty associated with the achievement of pure shear fracture limits is the crack opening modes, which generally occur near the transition region between uniaxial tension and in-plane shear conditions [103]. Furthermore, the double-notched shear (DNS) test is commonly used to determine fracture strains induced by crack opening through in-plane shear. It should be noted that this test does not strictly fulfill the conditions of pure shear due to the presence of bending effects and

the development of localized necking at the end of the testing process [104]. Roth and Mohr [105] proposed 600 distinct specimen geometries and demonstrated the value of using three instead of one type of shear specimen. Further insights on specimens implying shear fracture are detailed in Section 6.1.1.

4.4. Edge Cracks

The FLD is also not reliable in accurately predicting edge cracks on shear cut surfaces during component forming. The preparation of blank edges presents a wide range of possibilities, making it challenging to describe the reduced formability at the edge [21]. The stress state experienced at the blank edge is typically uniaxial, implying that it should undergo necking before fracturing under tension. However, due to the shearing process, the material properties and surface characteristics of blank edges are significantly altered. Consequently, the occurrence of fracture at the edge can vary depending on microscopic features or defects before the material reaches its actual necking limit [106]. Pre-forming is an important forming process in the prevention of edge cracking in flanging and edge stretching processes. Various process parameters in shear cutting have been identified to impact the residual formability of metallic materials. Nasheralahkami et al. [107] investigated the influence of die clearance on sheared edge quality, while Matsuno et al. [108] examined the impact of cutting edge geometry on residual forming capacity. Shih et al. [109] explored the effect of shear rake angle. Standardized experimental approaches are still necessary for successful inclusion of this effect into the modeling [21].

Frómeta et al. [110] demonstrated the reliability of the Essential Work of Fracture (EWF) methodology in assessing the fracture toughness of CP and DP steel grades to properly address issues associated with edge cracking. More recently, Feistle et al. [111] stated that it is imperative to use the GFLC to correctly take into account the introduced pre-forming in the formation of the Edge-Crack-Sensitivity Factor to be able to use it in the finite element simulation. Pre-deformation should not be considered as pre-damage, which would increase the edge crack sensitivity when using multi-phase steels [111].

4.5. Bending Influence

Traditional FLD determination is based on in-plane deformation, without taking bending components into account [112,113]. Hence, in situations where the strains on the outer layer surpass those of the membrane layers, the FLD fails to provide proper forming behavior results [21,114]. Although this is known and has not been a concern for many years, the advancement towards materials with higher strength/lower ductility, as well as lower post-necking plasticity, such as AHSS, accentuates the impact of bending on forming behavior.

Under superimposed bending, the FLD usually produces conservative results. This behavior arises from the fact that bending introduces a partially compressive stress state throughout the material thickness, which stabilizes the sheet and delays or prevents the onset of necking. When a material is subjected to bending in addition to other loading conditions, the conventional FLD often provides inaccurate results. In these contexts, materials exhibit a higher deformation capacity than indicated by the FLD, as major strain values located above the safety limit, are in reality, below the failure limit [21,115]. Research conducted by Kitting et al. [116] involved stretch–bending tests conducted on DP800 and CP800 steels under plane-strain and biaxial stretching conditions. The results revealed a significant underestimation of the forming potential of these materials by the traditional FLD in combined stretching and bending operations. However, it should be noted that under severe stretch–bending conditions, materials may experience surface failure, even if strains remain below the FLC [21].

Kitting et al. [115] proposed a phenomenological approach that offers the ability to predict stretch–bending formability using the conventional FLC prediction method. Neuhauser et al. [113] conducted angular stretch bending tests on DP600 steel and presented a methodology for quantitatively assess the formability of steel sheets subjected to

stretching with superimposed bending. They also demonstrated how to integrate these findings into the existing FLD framework. Despite the well-known relationship between instability and bending radius, this area of research has not yet reached full industrial maturity. Its development is crucial for achieving a comprehensive analysis of formability [21].

4.6. Ironing and Coining

Through-thickness compression in negative hydrostatic stress states is encountered during ironing and coining operations. As a result, the FLD is unable to correctly predict the component criticality, indicating premature failure [106]. Borrego et al. [117] evaluated the hole flanging operation through traditional FLD analysis. Their findings revealed that strain path curves for successful hole-flanged parts near the formability limit exceeded the limits defined by the FLC, yet no failure was observed. Alternatively, the Limiting Forming Ratio (LFR) is a more suitable measure of formability in conventional hole flanging operations. This parameter directly quantifies the maximum stretching of the material at the hole tip [117].

5. Constitutive Material Models

In sheet metal forming applications, an accurate representation of the material's plastic behavior is crucial for obtaining reliable results in finite element simulations [118]. The accuracy of finite element simulation strongly depends on the extent to which a material constitutive model can characterize the real material properties [119]. The plastic behavior of a material in a general stress state is described by three elements [120]:

- Yield Criterion;
- Associated Flow Rule;
- Hardening Rule.

Figure 9 presents an overview of the required material model parameterization concerning sheet metal forming simulation, while material model formulations applied to characterize material behavior in some representative studies focused on failure/damage models are reported in Table 4 Currently, constitutive models with anisotropic yield criteria based on the associated flow rule and isotropic hardening rule are extensively used in this field. However, the increased adoption of lightweight materials like AHSS and the growing demand for accurate simulation of forming behavior necessitate the development of more accurate constitutive material models. The selection of appropriate yield criteria and hardening rules, as well as the fitting of these models through suitable material testing procedures, is of significant importance in sheet forming simulations. Nevertheless, the adoption of the most advanced and comprehensive material model formulations is not always favored for predicting forming behavior. Factors such as cost, ease of implementation, and accuracy must be considered. Cost concerns mainly pertain to the mechanical testing required for model calibration, which explains the widespread utilization of Hill's 1948 model. Furthermore, the chosen model should gain industrial acceptance, with emphasis on computational efficiency, ease of implementation in numerical simulation codes, and user-friendliness. Ultimately, the accuracy of the model's predictions concerning the yield locus, uniaxial yield stress, and the coefficient of plastic anisotropy in uniaxial conditions must be guaranteed. Banabic [120] offers a comprehensive and historically detailed analysis of various material models, while a recent review paper written by Hou et al. [53] outlines the latest trends in material models addressing sheet metal forming applications.

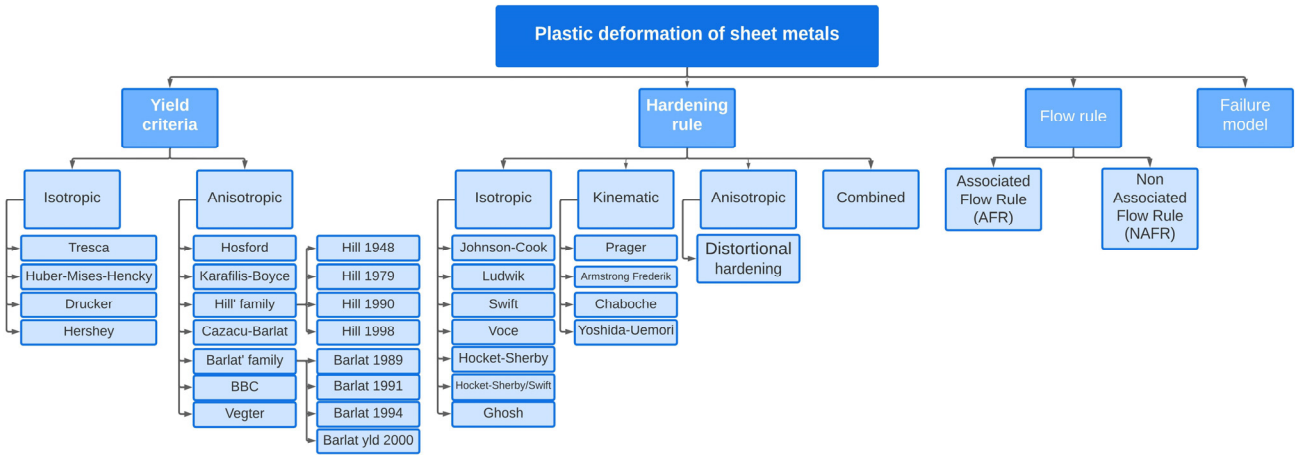

Figure 9. Summary of constitutive material models ([121–144]).

5.1. Yield Criterion

A yield criterion serves as a defining boundary that marks the transition from elasticity to plastic flow in response to various stress combinations [145]. Thus, accurately characterizing the yield surface is of significance, as sheet metal forming processes typically operate within the plastic region. Although high-strength sheets generally exhibit average r-values of 0.8–1.0, certain steels exhibit significant planar anisotropy r-values [146]. Anisotropic yield criteria are favored in material models for sheet metal forming operations during the production stage. The yield locus depicted in Figure 10a represents different forming states. The precision of the yield locus is a key indicator of the accuracy of failure/fracture prediction, making it vital for the sheet metal forming community to establish highly precise yield criteria. This precision is essential for effectively anticipating failures/fractures and preventing costly production mishaps [147].

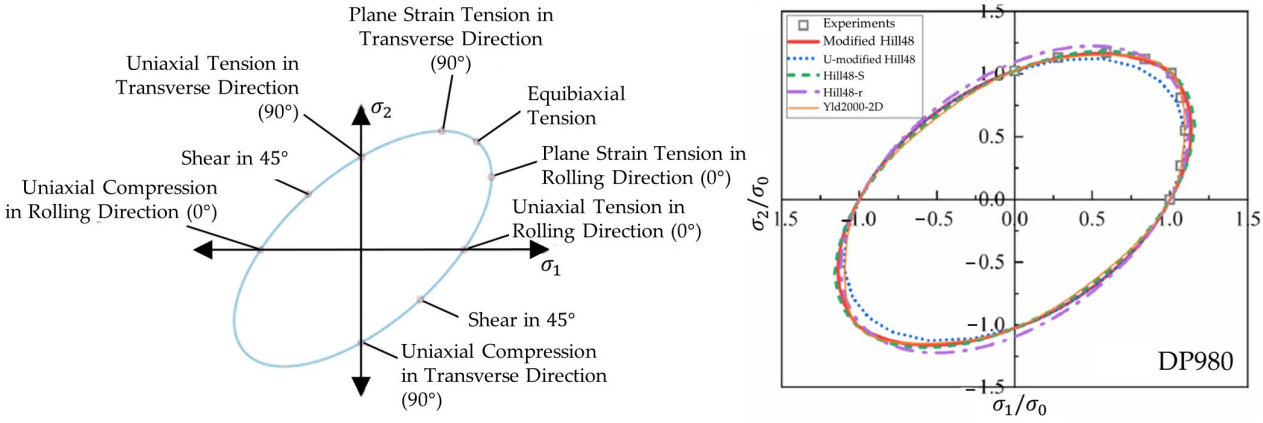

(a) **(b)**

Figure 10. (**a**) Different stress states identified on a yield locus representation. Reprinted from Ref. [148] with permission. Copyright 2016, Dr. Alper Güner. (**b**) Comparison of the yield loci proposed by different yield criteria, reprinted from Ref. [149] with permission. Copyright 2022, Elsevier.

Isotropic yield functions [121–126] are not commonly employed in the forming industry. Despite the widespread use of the Hill 1948 [127] anisotropic quadratic function due to its ease of parameter determination, it has limited capability in predicting sheet metal anisotropy accurately [146]. Non-quadratic functions, particularly the Hill 1979 [128] yield function, were proposed to address this limitation [120], although they are applicable only when principal stress directions align with orthotropic axes [120]. The emergence of lightweight materials like AHSS has led to more advanced formulations of anisotropic

yield criteria, such as Barlat [129–132], Banabic-Balan-Comsa (BBC) [133,134], Cazacu-Barlat [135], and Vegter [136,137] models, offering improved descriptions of the yield surface and better tracking of planar variation in uniaxial yield stress and plastic anisotropy coefficients [120]. Figure 10b depicts the yield locus of various yield criteria for a DP980 steel. The Barlat yld2000 model was used by Gutierrez et al. [150] for the analytical determination of forming limit curves in two 3rd generation AHSS steels. While these yield criteria successfully accounted for steels' anisotropy, they underestimated the yield stress under shear conditions. Yoshida et al. [146] developed a more advanced yield function that provides a more accurate description of anisotropy influence.

Table 2 summarizes the most commonly used yield criteria for sheet metal forming simulations and the corresponding mechanical property parameters. All models require measurement of the material's plastic anisotropy, serving as an indicator of sheet metal formability. Hill 1948 only requires standardized uniaxial tension along the rolling, diagonal, and transverse directions. Additionally, Barlat yld2000 and BBC2005 require biaxial tension. In its initial formulation, the Vegter material model also necessitated plane strain and shear tests in order to calibrate 17 parameters. However, Vegter 2017 [136] only requires standardized tensile tests.

Table 2. Overview of the essential parameters needed for the most common material models.

	Uniaxial Tensile Test				Biaxial Tension			FE Software		
	Plastic Anisotropy Coefficients	**Stress Coefficients**	**Tensile Strength**	**Uniform Elongation**	*	**	***	**AutoForm**	**LS-DYNA**	**Abaqus**
	r_0, r_{45}, r_{90}	σ_0, σ_{45}, σ_{90}	R_{m0}, R_{m45}, R_{m90}	A_{g0}, A_{g45}, A_{g90}	r_b	σ_b	**M**			
Hill 1948 [127]	X							X	X	X
Barlat Yld2000 [129]	X	X			X	X	X	X	* (Barlat2004)	
BBC 2005 [133]	X	X			X	X	X	X		
Vegter 2017 [136,137]	X		X	X				X		

* Biaxial Plastic Anisotropy; ** biaxial stress; *** standardized value.

The research conducted by Gösling [151] demonstrated that the Barlat yld2000 exhibits superior accuracy in predicting earing compared to the Hill 1948 material model, which is influenced by the yield strength in the diagonal direction. A comparative analysis of three different yield criteria, namely Hill 1948, Barlat yld2000, and Barlat yld2000-Var [152], was performed by Cheng et al. [153]. Among these, the third mentioned model provided more precise results addressing the hardening behavior and the forming limit curve, especially under biaxial tension stress states and the stretch formability. Another study conducted by Panich et al. also concluded the suitability of Barlat yld2000 in combination with the Swift hardening law to numerically determine FLC [154]. Moreover, it is worth mentioning that the Yld2004-18p yield function demonstrated superior performance in predicting the earing contour of a fully drawn cylindrical cup in comparison to Hill 1948 and Yld91 [155].

Regarding the future trends in yield criteria for sheet metal forming applications of AHSS, several directions can be identified. Firstly, there is a need for the development of new yield criteria aimed at improving flexibility and reducing the number of parameters and the required experimental tests [119]. Secondly, standardized shear and plane strain experimental tests need to be developed. Lastly, there is a growing interest in the development of crystal plasticity material models. According to Hou et al. [53], crystal plasticity material models are advanced multi-scale modeling approaches that capture the deformation behavior of polycrystalline materials by considering slip, twinning, and phase transformation processes.

5.2. Hardening Rule

The hardening laws play a crucial role in describing how the yield surface evolves under plastic deformation and various loading conditions. These laws can be categorized

into four main families [156]: (i) isotropic, (ii) kinematic, (iii) anisotropic; for example, distortional hardening, and (iv) combined. Isotropic hardening implies that the yield surface expands without changing its shape as plastic strain increases. Kinematic hardening maintains the shape of the yield surface while translating it in the direction of strain. Distortional hardening refers to the distortion of the yield surface shape during plastic deformation [157]. Combined hardening models, such as kinematic + isotropic or kinematic + distortional hardening, have also been proposed. Figure 11 illustrates the representation of the yield locus for these four different families of hardening rules.

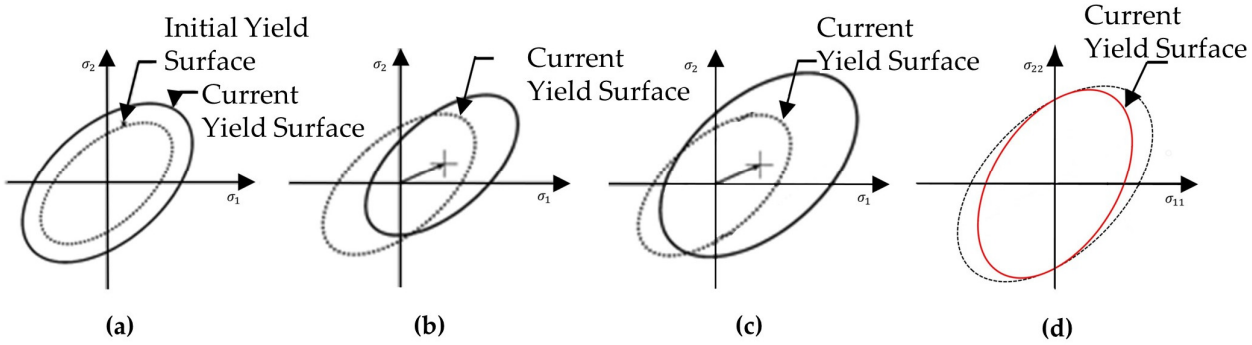

Figure 11. Schematic representation of the yield locus for: (**a**) isotropic hardening; (**b**) kinematic hardening; (**c**) combined hardening; (**d**) distortional hardening. Adapted from [158,159].

Typically, isotropic hardening models [138–140] are selected to reproduce the hardening behavior of metals in sheet metal forming processes due to its simplicity. However, experimental observations indicate that hardening behavior differs under various loading conditions and directions, even under proportional loading conditions [53,138,160,161]. Therefore, anisotropic hardening behavior cannot be described by anisotropic yield functions under isotropic hardening [161]. Moreover, cyclic loading and the Bauschinger effect, a material property affecting stress/strain characteristics under non-proportional loadings [53,119], are not accurately modeled by isotropic hardening laws, leading to inaccuracies in predicting forming behaviors, such as springback and tearing. Kinematic hardening models [141–144], like Prager's, Armstrong and Frederick's, and Chaboche's, along with distortional hardening models, such as HAH, offer improvements. Rosenschon and Merklein [162] have stated that a kinematic hardening law leads to a significantly better approximation of cyclic hardening behavior, rather than a pure isotropic formulation. Distortional hardening models, such as the Homogeneous Yield Function-based Anisotropic Hardening model (HAH), offer an advantage in that the expression and parameter calibration of isotropic and anisotropic hardening terms are independent from each other [53]. Zhu et al. [158] demonstrated that the HAH-2d model reasonably captures the Bauschinger effect but requires further improvements for cross-loading softening predictions. Combined ongoing efforts to refine material response under non-proportional loading conditions have been proposed, combining kinematic and distortional hardening models [163–165]. The work conducted by Yang et al. [166] provides prospective development directions with respect to anisotropic hardening modeling according to material and forming processes.

Butuc et al. [167] performed a comparative analysis of different hardening models to predict the FLC of DC06 steel. The right-hand side was well-predicted by all evaluated models. The left-hand side was overestimated by the Swift law and combined Swift/Armstrong–Frederik law. Dizaji et al. [168] adopted a similar approach but focused on the influence of different hardening models on ductile fracture criteria. Their results showed that the combined Chaboche–Zeigler hardening model [169] and the kinematic Zeigler–Prager equation [141] provided more accurate predictions for the fracture location in the square cup drawing using the Brozzo et al. [170] and Cockcroft and Latham [171] ductile fracture criteria, respectively. Nevertheless, the isotropic hardening model delivered better results than the kinematic hardening model for the Ayada et al. [172] ductile fracture criterion.

5.3. Flow Rule

Yield criteria can be formulated with the associated flow rule (AFR) and non-associated flow rule (NAFR). AFR models, such as Barlat yld2000, capture yield stress and strain rate ratio using a linear combination of two functions, suitable for high-strength steels. However, 3rd generation AHSS, such as Q&P steels, exhibit a strength differential effect that requires more advanced AFR yield functions, leading to higher complex formulations and computational costs [53]. NAFR offers a simpler approach for modeling anisotropic yield and plastic flow in metallic materials. It uses separate yield and plastic potential functions with simpler forms and analytical parameter calibrations. Stoughton's non-associative flow model [173], based on the Hill 1948 function, accurately predicts yield stress in strongly anisotropic materials. NAFR's usage and applications are increasing, as more research investigates its effectiveness [174–178].

6. Material Characterization Methods

In the realm of sheet metal forming processes, the material undergoes various types of loading. Accurate experimentation plays a significant role in accurately calibrating models that predict crack initiation on macroscopic features. The fracture models rely on the correct assessment of the fracture strain. These fracture models require experimental testing under different stress states to fully characterize fracture occurrence. Different sample geometries, test configurations, and/or loading paths generate different levels of stress states, which significant influence the fracture typology. In order to represent any stress state, two dimensionless parameters, namely the Lode Angle and the Stress Triaxiality, need to be represented. The loading path leading to fracture, represented in terms of the equivalent plastic strain evolution as a function of the Stress Triaxiality η and Lode Angle parameter θ, significantly influences the precise assessment of fracture initiation location. Therefore, a wide range of stress states need to be covered by employing diverse experimental tests. Lian et al. [179] proposed hybrid ductile damage modeling with a hybrid ductile experimental–numerical parameter calibration procedure specifically tailored to account for the damage characteristics of modern high-strength steels. Figure 12 presents the methodology followed by the authors to calibrate material and fracture parameters based on experimental tests. Although the knowledge of the strain to fracture is the main ingredient of damage models [180], they used a phenomenological model to characterize the onset of damage; the crack initiation strain, rather than the fracture strain.

Figure 12. Methodology followed by Lian et al. [179] for material and fracture model parameter calibration.

Currently, most material characterization methods are based on the assumption of proportional loading histories. Figure 13 presents some conventional experimental techniques employed for the assessment of relevant data such as fracture strain, η, and θ. However, the achievement of proportional loading conditions at the specific material point where fracture initiates proves to be challenging. Thes sample geometry and test configuration often induce a certain level of deviation from linearity during ductile fracture. Furthermore, non-linear deformation paths commonly arise in multi-forming operations. As such, methods capable of characterizing the stress state under non-proportional loading are needed. The current trends in material characterization methods rely on the industrial standardization of fracture limits determination and the enhancement of material assessment techniques for both proportional and non-proportional loading histories. Table 4 provides a review of the material characterization methods employed to calibrate fracture/damage models parameters.

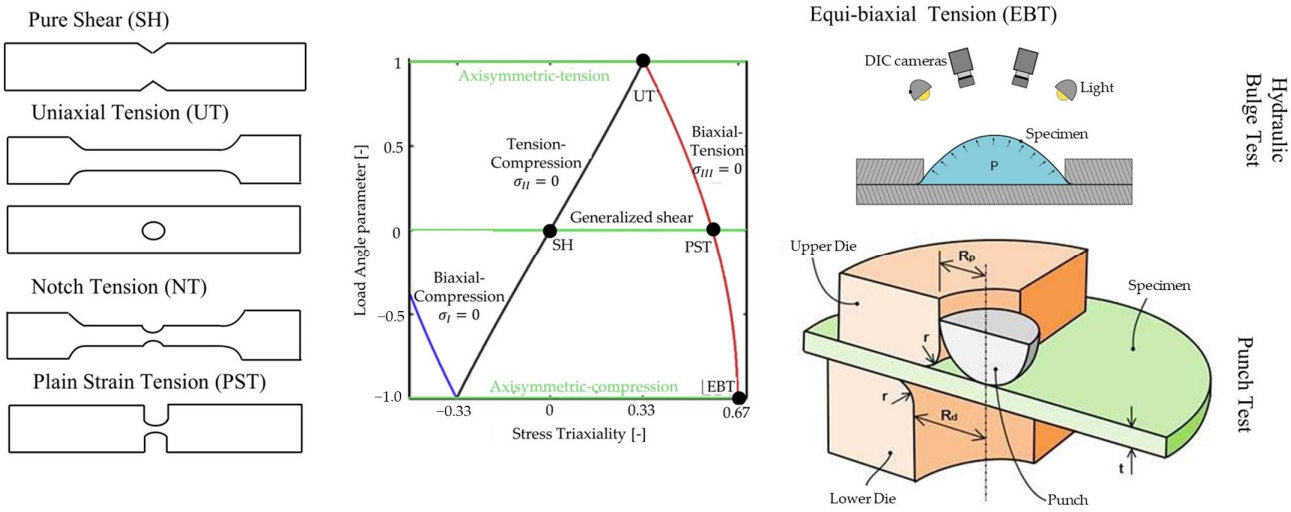

Figure 13. Load angle parameter as a function of stress triaxiality for plane stress conditions and conventional specimens over a wide range of stress triaxialities: pure shear, uniaxial tension, notch tension, plane strain tension, and equi-biaxial tension. Reprinted from: Ref. [181], open access; Ref. [182] with permission, copyright 2017, Elsevier; Ref. [183] with permission, copyright 2016, Elsevier.

6.1. Proportional Loading

6.1.1. Pure Shear ($\eta = 0; \overline{\theta} = 0$)

The accurate assessment of the shear fracture limit is currently one of the most questioned subjects in sheet metal fracture modeling. Over the years, a large amount of sample geometries and methods have been proposed to address this issue. On one hand, the ability of metallic materials to undergo shear deformation facilitates the attainment of elevated levels of plastic strains. On the other hand, this makes it more difficult to achieve pure shear deformation paths at the crack initiation location.

Miyauchi [184] introduced the initial planar shear test documented in the literature. The specimen comprises two symmetrically sheared regions, and it is subjected to an axial load [185]. Rauch and G'Sell [186] adopted a modified version of this test, which was further refined by Genevois [187]. In Genevois's test, the rotation of the specimen under the influence of shearing forces is impeded by a highly rigid frame. The specimens employed in this test possess a simple rectangular shape, which deforms into a parallelogram. Bouvier et al. [185] conducted an optimization of the mechanical test, focusing on the impact of sample geometry and setup configuration on stress and strain uniformity. Subsequently, the ASTM-B831 [188] standard test method was established for shear testing, proposing a novel sample geometry and loading conditions. Alternative shear specimen designs have also been proposed, such as the symmetric double-shear specimen with two identical gage sections [189]. However, the application of these specimens is limited due to the

interference of edge effects when calculating shear stress [53]. It is important to note that the aforementioned approaches were originally devised for the determination of plastic hardening and are not generally suitable for characterizing formability limits caused by fracture [190]. Furthermore, they are affected by fracture occurrence at the free edges.

The primary prerequisite for determining the fracture limit strain in shear tests is the ability to achieve pure shear deformation paths, thereby ensuring consistent zero triaxiality throughout the entirety of the experiment. To achieve this goal, it is essential to assure homogeneous stress and strain distribution while also preventing crack initiation at free edges, which can prove to be challenging, as most of the materials exhibit higher strain to fracture under uniaxial tension rather than pure shear. The importance of this lies in the likelihood of crack initiation occurrence at higher stress triaxialities. Iosipescu [191] was among the first to endeavour the development of a pure shear test with constant triaxiality evolution. The subsequent ASTM D5379 [192] standard was formulated based on Iosipescu's work, and it is predominantly employed for composite materials. However, both approaches fail to adequately address the issue of edge cracking, similar to the specimens proposed by Bao and Wierzbicki [193] and Shouler and Allwood [194]. Dunand and Mohr [195] introduced a novel specimen, incorporating localized sheet thickness reduction. Nevertheless, the initiation of fracture into this specimen could be reliably guaranteed to commence precisely at the center of the sheared zone, thus compromising the achievement of triaxiality constancy. Figure 14 illustrates the four aforementioned proposed specimens. More recently, Khameneh et al. [196] investigated the fracture behavior of DP1180 steel. The two adapted geometries tested based on the Shouler and Allwood [194] and Peirs et al. [197] specimens did not deliver pure shear deformation paths. The former specimen exhibited an average triaxiality value of approximately 0.15, whereas the mini-shear geometry inspired by Peirs et al. [197] maintained a triaxiality value of approximately 0.20. It is important to mention that the aim of the authors was to accomplish a strain path evolution between pure shear and uniaxial tension, which was successfully achieved by the two proposed specimens.

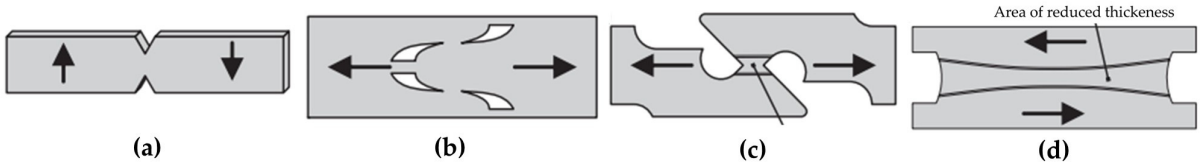

Figure 14. Shear test specimens proposed by [190]: (**a**) Iosipescu [191]; (**b**) Shouler and Allwood [194]; (**c**) Bao and Wierzbicki [193]; (**d**) Dunand and Mohr [195]. Reprinted from Ref. [190].

Significant developments have been made in addressing the need for more accurate pure shear strain deformation paths through adapted in-plane torsion tests. These tests offer the capacity to achieve maximum strains up to 1.0 [198]. In the context of in-plane torsion testing, a circular sheet sample is clamped at both the outer rim and in the center. By inducing planar rotation of the outer fixture, a simple shear is applied to the circular region situated between the clamps [199]. Yin et al. [190] determined the fracture strains for DP1000 using an in-plane torsion test, with a grooved specimen free of slits. This test configuration facilitated fracture propagation under constant zero triaxiality and effectively mitigated incipient cracking arising from edge effects. Grolleau et al. [200] proposed an alternative clamping system, featuring a highly rigid device for in-plane torsion testing using grooved specimens. The system allowed for full optical access to the specimen's gage section, enabling DIC measurements. It provided an almost perfectly proportional loading path for simple shear loading, making it suitable for cyclic loading as well as testing ultra-high strength steels. Moreover, Roth and Mohr [183] recently reported a geometry shape optimization procedure that effectively addressed the strain to fracture under pure shear. The smiley shear specimen, depicted in Figure 15a, is distinguished by a series of

notches that define the contours of the shear gage sections. As observed in Figure 15d, a more linear strain path evolution is achieved.

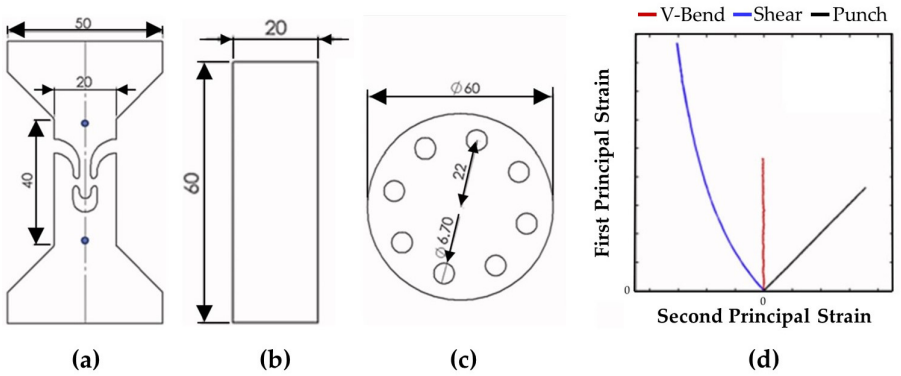

Figure 15. Roth and Mohr [183] novel proposed specimens to address fracture limits under: (**a**) in-plane shear; (**b**) plane strain tension; (**c**) equi-biaxial tension; and (**d**) evolution of the principal strain paths in the major vs. minor space. Reprinted from Ref. [183] with permission. Copyright 2016, Elsevier.

6.1.2. Uniaxial Tension ($\eta = 1/3; \bar{\theta} = 1$)

ASTME-8 outlines the procedure for conducting uniaxial tensile tests on metals at room temperature, enabling the determination of mechanical properties [201]. The amount of plastic deformation achievable through the uniaxial tensile test is typically limited to around 20–30%, which is noticeably lower when compared to other stress states such as shear. Uniaxial tensile tests are usually performed in three directions, rolling, transverse, and diagonal, to investigate material anisotropy. The mechanical properties obtained from uniaxial tensile testing include Young Modulus, Yield Strength, Tensile Strength, Uniform and Total Elongation, and r-values. When measuring the fracture strain under uniaxial tension using the conventional flat dog-bone specimen, the stress state undergoes changes during the loading process. To measure the limit strains under uniaxial tension, a tensile specimen with a central hole can be used instead, which offers the advantage of maintaining a more constant linear strain path until fracture occurs near the hole boundary [202]. However, careful selection of the hole manufacturing process as well as hole diameter dimension is relevant, as inadequate choices can lead to significant errors in the estimated strains to fracture for uniaxial tension [183]. Conversely, the work conducted by Behrens et al. [88] reveals that the central hole specimen yields non-linear strain path histories.

6.1.3. Notch Tension

In order to encompass a wider spectrum of stress triaxiality values along the fracture locus, the utilization of notch tension is frequently employed. By adjusting the notch angle and size on notched flat specimens, a diverse range of stress triaxiality conditions can be attained [203]. The presence of notches ensures the development of a localized neck at the center of the specimen, perpendicular to the loading axis [202]. For instance, notch tension tests have been proposed to calibrate the parameters of the extended Modified Mohr Coulomb model (eMMC) [204,205].

6.1.4. Plane Strain Tension ($\eta = 1/\sqrt{3}; \bar{\theta} = 0$)

Fracture occurrence during plane strain tension is primarily attributed to the load carrying capacity in the out-of-plane shear direction. Various approaches have been employed to determine the strain limits under plane strain tension. Jia and Bai [205] utilized uniform plane strain specimens as well as butterfly-shaped specimens. Santos et al. [206], on the other hand, employed double-notched specimens to assess the deformation mode under plane strain tension. However, it should be noted that with these test configurations, the stress state leading to fracture may not remain constant. The point at which the plane strain

tension limit is typically reached is on the material surface during bending operations. To address this, Roth and Mohr [183] introduced a modified plane strain bending configuration capable of delivering proportional loading histories (Figure 15d). Their V-bending experiment involves placing a rectangular sheet material coupon (Figure 15b) on top of two parallel rollers. The sheet specimen is then subjected to loading by two parallel rollers through a thin, knife-like tool, which remains stationary, resulting in the formation of a shar V-bend.

6.1.5. Equi-Biaxial Tension ($\eta = \frac{2}{3}; \overline{\theta} = -1$)

Fracture testing of sheet materials under equi-biaxial tension is well-standardized [183]. Usually, either the bulge test or the punch test is used. The hydraulic bulge test involves the deformation of a flat specimen through the application of hydraulic pressure. The outer edge of the sample is firmly clamped with a circular die, while the internal area is subjected to increasing fluid pressure during the test, causing deformation until fracture occurs [181]. The ISO 16808 standard [207] specifies a method for determining the biaxial stress–strain curve using an optical measuring system. The bulge test allows for a much larger achievable strain prior to necking, owing to the nearly equi-biaxial stress state, compared to the uniaxial tensile test. The punch test, on the other hand, utilizes a miniature disc sample subjected to compressive force applied through a hemispherical punch indenter on the upper surface of the disc [208]. The small punch deformation test procedure for metallic materials is covered by the standard ASTM E3205-20 [209]. The configuration used to perform both tests is schematically presented in Figure 13. The punch test offers the advantage of avoiding the evacuation of excess fluid after fracture, although the presence of tool friction can influence the experimental results. Roth and Mohr [183] proposed an adaptive punch testing procedure, wherein the distinctive feature is that the punch remains stationary throughout the experiment, while the die and clamping plate move downwards. The specimen geometry is presented in Figure 15c. This approach reduces the required focal depth of the DIC camera system, enabling shorter object distances and ultimately enhancing the spatial resolution of the acquired surface strain fields. Furthermore, the location of fracture initiation remains fixed throughout the entire experiment.

6.1.6. Butterfly Test

Mohr and Henn [210] devised a butterfly-shaped specimen that facilitated the examination of fracture behavior under low and intermediate stress triaxialities, ranging from 0.0 and 0.6. The generation of different stress triaxialities can be accomplished without altering the design or dimensions of the specimen but rather by adjusting its orientation. The experimental procedure is conducted using a biaxial testing apparatus comprising a fixed portion, a vertically movable portion, and the corresponding specimen. By adjusting the angle between the specimen axis and the vertical axis, different stress triaxialities can be achieved. The gage section of the specimen exhibits a uniformly reduced sheet thickness compared to its boundaries, and it is designed to induce crack formation at the center of the specimen. Bai [211] introduced modifications to the design of the gage section, resulting in a non-uniform sheet thickness within the gage section.

Dunand and Mohr [195] further improved the initial specimen design, attempting to increase homogeneity of the stress state and strain fields at the specimen center. Additionally, the configuration of the testing setup enabled the application of combined normal and shear loads, as illustrated in Figure 16a. The experimental investigation focused on TRIP780 steel, encompassing a range of loads from pure shear to transverse plane strain tension. The findings revealed that under shear loading, both stress triaxiality and Lode angle parameter exhibited relative constancy. However, a linear increase in stress triaxiality after the onset of through-thickness necking was observed for tension loading. Moreover, a high sensitivity to imperfections in the specimen geometry was noticed.

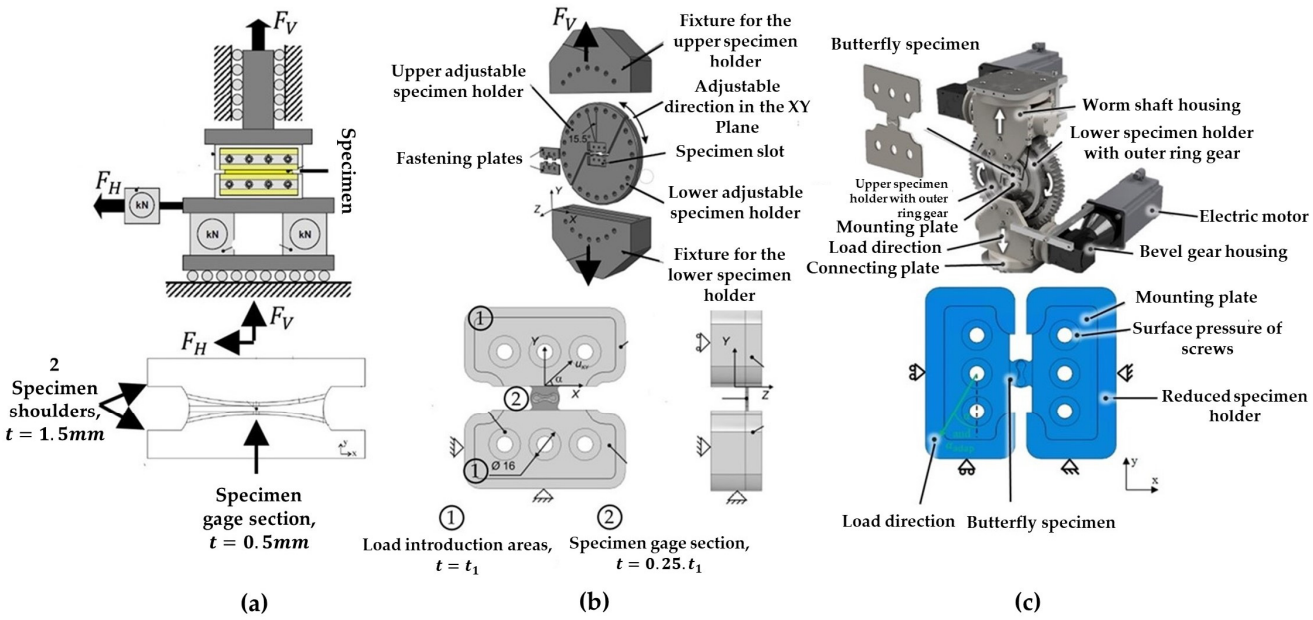

Figure 16. Specimen shape and experiment test configuration setup proposed by: (**a**) Dunand and Mohr [195], dual actuator system; reprinted from Ref. [195] with permission, copyright 2011, Elsevier; (**b**) Peshekhodov et al. [212], tensile testing machine; reprinted from Ref. [212], open access; (**c**) Stockburger et al. [213], tensile testing machine; reprinted from Ref. [213], open access.

Despite the improvements made to the initial butterfly specimen design proposed by Mohr and Henn [210], achieving uniform stress and strain distribution throughout the entire experiment, especially under shear-dominated loading conditions, remained challenging. Therefore, Peshekhodov [212] further enhanced the butterfly design with the aim of ensuring strain localization at the specimen's gage section, regardless of the applied load direction. The new specimen geometry was divided into three areas, as illustrated in Figure 16b. Comparative FEM analysis between this new geometry and the one proposed by Bai [211] demonstrated an increased likelihood of fracture initiation at the desired central area under arbitrary stress states. Furthermore, a more precise definition of the stress state could be achieved by specifying the load application angle. The implemented apparatus, based on a single material characterization technique, facilitated the generation of a wide range of stress triaxialities, from pure shear to plane strain tension. This approach accurately modeled the fracture behavior of DP600 steel using the CrachFEM and MMC fracture models.

Behrens et al. [88] adopted a similar experimental and numerical approach to obtain fracture data for CP800 steel and calibrate the MMC fracture model. Similarly, the butterfly specimen developed by Peshekhodov [212] demonstrated fracture initiation at the specimen center under various stress triaxialities, ranging from shear to uniaxial tension. Although the butterfly specimen did not deliver entirely proportional strain paths, improvements compared to other experimental tests are undeniable. In order to solve the problem of non-linear strain path evolution, Stockburger et al. [213] proposed an innovative adaptive experimental configuration, as shown in Figure 16c. The key feature of this setup was the continuous real-time adjustment of the loading angle to maintain constant stress states. To achieve this, Phyton script was incorporated into the numerical simulation, compensating for deviations in stress triaxiality exceeding 0.03. A comparative analysis between the calibration of the MMC fracture model using the new adaptive test methodology and the fixed loading angle approach revealed significant enhancements in achieving linear strain paths. Furthermore, as the strain paths became more consistent, the equivalent plastic strain at fracture increased.

6.2. Non-Proportional Loading

In the context of sheet metal forming operations, the presence of non-linear strain path histories at fracture initiation sites has been a frequent phenomenon. Hence, attention within the sheet metal forming research community has also been directed towards enhancing experimental methodologies capable of generating controlled non-linear strain paths, further improving the accuracy of material fracture and failure modeling. Aisvaran [214] identified the main test procedures to generate non-linear strain paths: (i) the Nakazima test with modified punch geometry; (ii) two step drawing; (iii) in-plane biaxial test with cruciform specimen; (iv) Bulge test with stepped dies; (v) cruciform specimen in conventional Nakazima test setup. Table 3 summarizes the main approaches for generating NLSPs tested on AHSS.

Table 3. Summary of non-linear strain path generation by different test procedures applied on AHSS.

Authors	Material	Procedure:		Findings:
				Two Step Drawing
Gaber et al. [215]	DP600	Two-step deep-drawing operation: non-linear strains are generated with an asymmetrical punch attached to the upper die that draws the blank over an elliptical shaped counterpunch located on the lower die.	The strain path is changed by using a different specimen geometry.	The Generalized Forming Limit Curve (GFLC) and the Time-Dependent Evaluation Method (TDEM) showed good predictive accuracy to model the Non-Linear Strain Paths (NLSPs) introduced by the experimental two-step drawing setup.
				In-plane biaxial test with cruciform specimen
Song et al. [216,217]	DP600	A circle arc profile is adopted in the thickness direction of the circular reduced zone to generate strain localization at the central point of the cruciform specimen. Six slots are added at each arm and the arrangement of slots is optimized.	The strain path during the test can be directly controlled by the motion of actuators along the two axes, which is sufficient to cover the whole forming limit diagram under linear and non-linear strain paths. The strain path changes in the central area of the cruciform are accomplished simply by changing either independent actuators' speed or loading directions in a single procedure without unloading. Two NLSPs are induced: (i) uniaxial tension followed by equi-biaxial stretching; (ii) equi-biaxial stretching followed by plane strain tension.	Strain path changes in the fracture initiation site are experimentally observed. The strain path change has almost no effect on the forming limit strains at fracture. The Oyane ductile fracture criterion predicts the experimental results under different strain paths.
				Nakazima test with modified punch geometry
Saxena et al. [218]	DP600	Nakazima test with modified punch geometry.	The strain path is changed by using an adapted punch geometry with two tailored patterns. The use of different specimen widths allows for the coverage of a wide range of major vs. minor principal strains' spectrum.	The experimental biaxial formability test revealed strain path modification: plane strain followed by equi-biaxial. The material formability was reduced by the introduction of strain path deviation. The NLSPs negatively affected the drawability and stretchability of the material.
Panich et al. [93]	DP590			The generated FLC based on the conducted procedure revealed decreased material formability. Experimental Fukui stretch drawing tests have shown a better predictive accuracy of the FLC generated by NLSPs rather than the conventional FLC.

The Nakazima test with modified punch geometry offers the advantage of achieving non-linear strain paths in a single-step procedure. Saxena et al. [89] designed five novel

punch geometries to replace the conventional hemispherical punch in order to change the strain path during deformation at the necking initiation site. In the work conducted by Drotleff [219], the FLC generated by the Nakazima test with modified punch geometry delivered better agreement in predicting the onset of localized necking of a Mini-Tunnel component compared to the analysis through the conventional FLC. The Nakazima test, employing a cruciform specimen, serves as an alternative technique to generate NLSPs. An innovative procedure proposed by Jocham et al. [220] incorporates a modified blank-holder with adjustable draw bead height, simplifying the need for a single specimen geometry to produce the FLC [220], as opposed to the two-step drawing approach, which requires varying specimen geometry [215]. He et al. [221] introduced an innovative test procedure designed to facilitate continuous non-linear biaxial tensile deformations of sheet metals via bulging with stepped dies. This bulging process lead to a distinctive change in curvature radius relative to the bulging height, and as the difference between successive elliptical sections increases, the presence of NLSPs becomes more pronounced [147]. The main distinctive feature of the in-plane biaxial test with a cruciform specimen is that it provides a frictionless way of investigating the strain path change in a cruciform specimen. The design of this specimen continues to undergo refinement within the scientific community; yet, standardization has not been established.

6.3. Finite Element Modeling: Validation and Verification

Employing finite element simulations within the sheet metal forming industry offers significant advantages over the trial-and-error approach to optimization. This methodology supports manufacturability, leading to heightened efficiency and a mitigation of both time and cost constraints. The validation of numerical models necessitates an evaluation of their precision through comparison of their outcomes with empirical observations from experiments. This validation holds true for both the calibration of constitutive fracture models via material characterization techniques and for verifying the accuracy of models in real-world components.

When conducting finite element modeling and parametrizing experimental methods, it is common practice to leverage symmetrical relationships. This involves modeling specimens using half or even one-eighth of the actual specimen, particularly in cases of shear, notch, and tension specimens, aiming to reduce CPU time. As a result, symmetrical boundary conditions must be applied. Mesh considerations with respect to mesh element type, element size sensitivity, and mesh refinement are also factors influencing post-processing outcomes. Table 4 presents the mesh element types employed in some material characterization methods published over the past 15 years for calibrating constitutive fracture/damage models.

The selection of 3D elements is preferred over shell elements, as the latter often yield inaccurate post-necking onset due to their inability to capture three-dimensional mechanical fields within localized neck regions throughout the thickness. In Abaqus v.2020 software, common approaches opt for 3D, C3D8R mesh element type, whereas when using LS-Dyna hexahedral fully integrated solid elements are used The work conducted by Pack and Mohr [222] significantly advanced numerical simulation modeling using shell elements. Their study introduced the Domain of Shell to Solid Equivalence (DSSE) in combination with the Hosford–Coulomb fracture model, validating the suitability of shell elements. Afterwards, Pack et al. [223] further confirmed the utility of shell elements, not only in fracture prediction but also in modeling through-thickness necking.

Determining the optimal element size typically involves conducting mesh sensitivity analysis. This analysis entails comparing the load–stroke curves obtained from different element sizes. In this context, mesh sensitivity analysis aims to obtain a close match of the simulated load–stroke curves between different element size meshes. Wang et al. [224] adopted this approach. Only then, can one move to the next step of calibrating the constitutive material model parameters. Frequently, element sizes of 0.1 mm are chosen, particularly in regions with concentrated deformation. Furthermore, employing data from

DIC systems can enhance the accuracy of element sizing. It is recommended to match the characteristic element length with the DIC facet size in order to avoid mesh size-dependent fracture behavior.

Mesh refinement is typically focused on the region where deformation is concentrated within the specimen. Additionally, increasing the number of element layers along the thickness direction is often adopted to enhance accuracy. As a rule of thumb, a finer mesh corresponds to a closer match between numerical and experimental load–stroke responses. For instance, in the study conducted by Roth and Mohr [183], numerical tests on punch and V-bending resulted in a fracture region element size of 100 µm. Specifically, when modeling specimens with significant out-of-plane deformation, such as in punch tests using 2D elements, increasing through-thickness integration points is pursued to improve accuracy. Recent advancements proposed by Cherouat et al. [225] have shown the effectiveness of 3D adaptive remeshing. Constantly optimized element quality as well as adaptive mesh refinement, either in the whole model or within the crack zone, have led to improved predictions of forming behavior, fracture, and damage evolution in sheet metal forming processes.

As explicit solvers are commonly employed, material density can be scaled such that a total amount of time steps are performed to solve the boundary value problems [226]. Moreover, physical time scaling and both homogeneous and mass scaling are managed to control CPU time. Sandin et al. [227] used explicit time integration to efficiently handle the high non-linearity caused by material fracture and element erosion.

In validation experiments, certain assumptions are made to streamline the process. Tools are considered rigid, meaning that they are undeformable. Occasionally, the contact between specimens and tools is assumed to be frictionless. These assumptions serve to simplify the complexity of the models as well as reduce CPU time.

Table 4. Summary of fracture/damage models applied on AHSS: stress states covered in experimental/numerical parameter calibration processes, validation experiments employed, and finite element modeling (comprising the period: 2010–2023).

Ref.	Material	Fracture/ Damage Model	Software	Material Model and/or Fracture Model Calibration								Forming Validation	
				Material Model			Stress States (Number of Specimens)						
				Yield Function	Hardening Rule	Flow Rule	Pure Shear	Uniaxial Tension		Plane Strain Tension	Equi-Biaxial Tension	Mesh/ Element Type	Experiment	Mesh/ Element Type
[204]	TRIP690	MMC	Abaqus Sub-routine	Hosford Non-Quadratic	Hollomon		**(1)**	**(1)**	**(1)**	**(1)**	**(1)**	2D		
[228]	DP780	MMC	Abaqus Sub-routine	Hill 1948	Swift - Piece-Wise Linear Curve	AFR	**(1)**	**(1)**	**(1)**	**(1)**	**(1)**		Stretch–Bending Test	3D/ C3D8R 2D/ S4R Plane Strain/ CPE4R
[101]	TRIP690	MMC	Abaqus Sub-routine	Von-Mises	Isotropic	AFR							Circular/Square Punch Tests	2D/S4R
[229]	TRIP780	MMC		Hill 1948	Isotropic	NAFR	**(1)**		**(1)**	**(1)**	**(1)**	3D/ 8-nodes	Butterfly Tests Central Hole Tension Notch Tension	3D/ 8-nodes
		Shear modified Gurson Model					**(1)**		**(1)**		**(1)**			
[230]	TRIP700	GTN	LS-Dyna					**(1)**					Cross Die Part	
[231]	two CP	CrachFEM	LS-Dyna	Hill 1948	Isotropic-Kinematic								Rectangular Deep Drawing Tests	
[179]	DP600	Bai–Wierzbicki + CDM	Abaqus Sub-routine	Bai-Wierzbicki	Isotropic	AFR	**(1)**	**(2)**	**(3)**	**(5)**	**(1)**	3D/ C3D8R		
[30]	DP600	Cockroft-Latham (CL) extended Cockroft-Latham (eCL) Johnson-Cook (JC) MMC	LS-Dyna	Yld2003	Isotropic-Kinematic	AFR	**(1)**	**(1)**	**(1)**			2D/ Quadrilateral	Nakazima Test Stretch Test	2D/ Quadrilateral
[232]	DP590	HC	Abaqus	Quadratic	Swift-Voce	NAFR		**(2)**	**(2)**			3D		
[233]	DP590 DP780 TRIP780	HC	Abaqus Sub-routine	Von-Mises	Isotropic	NAFR	**(1)**	**(2)**	**(2)**		**(1)**	3D		

Table 4. *Cont.*

Ref.	Material	Fracture/ Damage Model	Software	Material Model and/or Fracture Model Calibration								Forming Validation	
				Material Model			Stress States (Number of Specimens)						
				Yield Function	Hardening Rule	Flow Rule	Pure Shear	Uniaxial Tension		Plane Strain Tension	Equi-Biaxial Tension	Mesh/ Element Type	Experiment	Mesh/ Element Type
[183]	DP780	HC	Abaqus Sub-routine	Von-Mises	Swift-Voce	NAFR	**(1)**	**(2)**	**(1)**	**(1)**	**(1)**	3D/ 8-nodes		
[234]	DP800	GISSMO	LS-Dyna	J2 plasticity	Isotropic	AFR	**(2)**	**(2)**	**(1)**		**(1)**	2D		
[205]	TRIP780	eMMC	Abaqus Sub-routine	Yld2000	Swift		**(1)**	**(1)**	**(1)**	**(2)**	**(1)**	2D/ S4R		
[235]	TRIP780	eMMC	Abaqus Sub-routine	Yld2000				**(1)**	**(1)**		**(1)**			
[236]	DP600	MMC	Abaqus Sub-routine	Hill 1948	Swift-Hocket-Sherby								Deep-Drawing Test	3D/ C3D8R
[43]	DP780	Johnson-Cook / GTN	Abaqus		Swift			**(1)**			**(1)**		Nakazima Test	2D/ S4R
[237]	DP1000	GISSMO	LS-Dyna	Hill 1948	Swift-Hockett-Sherby		**(1)**	**(1)**		**(1)**	**(1)**	2D	Cross Die Part	
[222]	DP780	DSSE + HC	Abaqus Sub-routine	Von-Mises	Swift-Voce	AFR		**(1)**		**(1)**			Notch Tension	2D/ S4R
													Equi-biaxial Punching	2D/ S4R
													Stretch–Bending Test	2D/ S4R
													V-Bending Test	
[223]	DP980	DSSE + HC	Abaqus Sub-routine	Von-Mises	Swift-Voce	AFR	**(1)**	**(1)**	**(1)**	**(1)**	**(1)**	2D/ S4R	V-Bending Test	2D/ S4R
													Notch Tension	2D/ S4R
													Stretch–Bending Test	2D/ S4R
													Punch Test	2D/ S4R
													Simple Shear Test	2D/ S4R
[238]	980GEN3	GISSMO	LS-Dyna	Von-Mises			**(1)**	**(1)**		**(1)**	**(1)**	2D		

Table 4. *Cont.*

Ref.	Material	Fracture/ Damage Model	Software	Material Model and/or Fracture Model Calibration									Forming Validation	
				Material Model			Stress States (Number of Specimens)					Mesh/ Element Type	Experiment	Mesh/ Element Type
				Yield Function	Hardening Rule	Flow Rule	Pure Shear		Uniaxial Tension	Plane Strain Tension	Equi-Biaxial Tension			
[239]	DP500	GTN	Abaqus								(1)	3D/ C3D8R		
[226]	DP980 CP980 CP1180	HC	Abaqus Sub-routine	Von-Mises	Swift-Voce	NAFR	(1)		(2)	(2)	(1)	3D		
[240]	DP780 DP980	GTN		J2 Plasticity	Ludwig				(1)				PreStraining + Stretch–Bending Test PreStraining + Hole Expansion Test	3D
[241]	DP1000	Bao-Wierzbicki Max shear					(2)		(1)				Deep-Drawing Test	
[227]	CP1000HD	MMC + GISSMO	LS-Dyna	Steibler plastic hardening model						(1)		3D/ 8-nodes hexahedral	Bending Test DENT Notch Tension Central Hole Tension In-plane shear	
[88]	CP800	MMC	Abaqus	Hill 1948	Hockett-Sherby		(3)	(2)	(3)	(2)	(1)	(1)	3D/ C3D8R		
[242]	DP980 DP1180	MMC	Abaqus Sub-routine	Hill 1948	Swift		(1)		(1)				Stretch–Bending Test Nakazima Test	
[224]	QP980	Brozzo Oh Rice-Tracey Ko-Huh DF20120	Abaqus Sub-routine	Drucker	Swift-Voce		(1)		(2)		(1)		3D/ C3D8R		
[196]	DP1180	MMC MMC + GISSMO	LS-Dyna	Yld 2004	Modified Hockett-Sherby		(1) (1)	 (1)	(1) (1)		(1) (1)	(1) (1)	3D/ Hexahedral		
[243]	DP600	HC	Abaqus Sub-routine	Von Mises	Swift-Voce	AFR	(1)		(2)	(1)			3D/ C3D8R	Hole Expansion Test	3D/C3D8R

7. Damage and Fracture Models

The incorporation of damage or fracture models holds substantial significance within the realm of sheet metal forming simulations, enabling the anticipation of fracture occurrences in industrial contexts, as well as facilitating a comprehensive understanding of damage behavior. These models can be systematically classified into two principal categories, namely coupled and uncoupled, each grounded either in micromechanical or phenomenological foundations. Figure 17 provides an overview of the classification of ductile fracture models and showcases various models within their respective family backgrounds. The fundamental divergence between coupled and uncoupled models resides in the former's integration of damage mechanisms alongside elastic and/or plastic responses, as opposed to the latter, which distinctly segregates damage evolution from material behavior. Furthermore, the domain of coupled models can be further bifurcated into micro-mechanical-based models and continuum damage models (CDMs). The former considers the deterioration of materials during the loading process, attributed to damage propagation, while the later finds its underpinning in a thermodynamic framework and is formulated upon a phenomenological basis. Table 4 summarizes the application of fracture/damage models on AHSS, referencing representative experiments to validate the models' suitability.

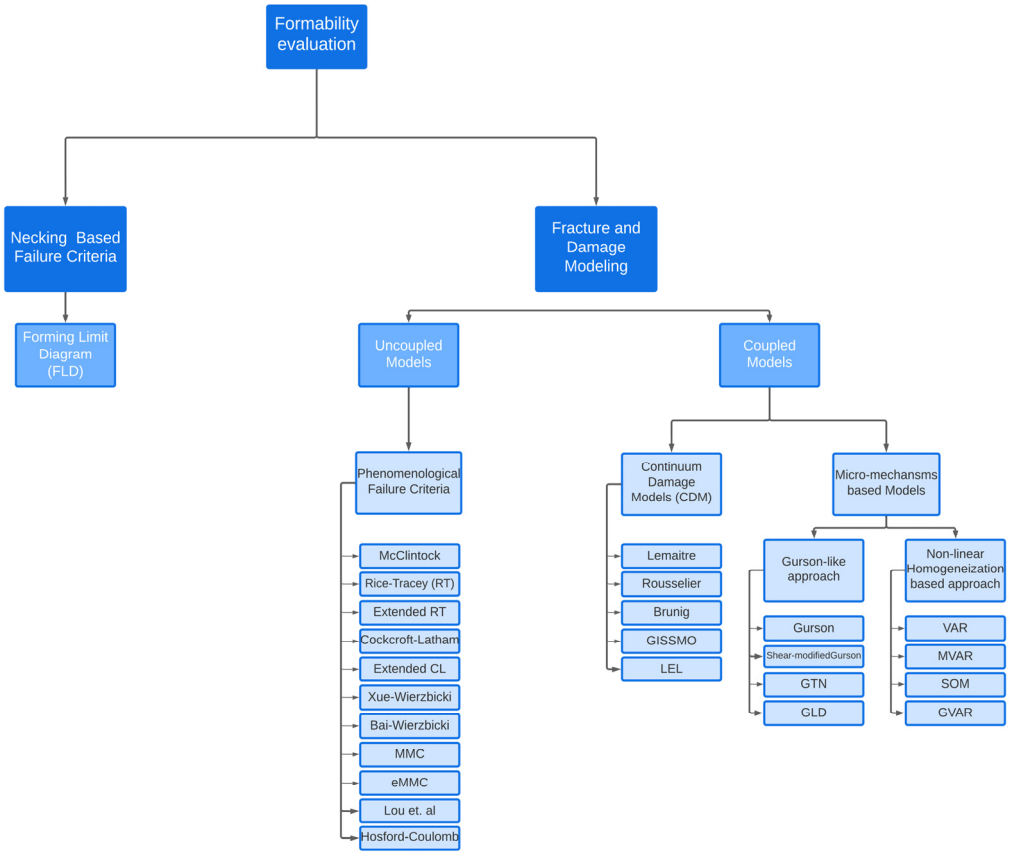

Figure 17. Ductile fracture models' classification and some representative models [178].

Damage and fracture models or fracture criteria operate by employing an accumulating damage parameter, which serves as a fundamental basis for assessing fracture. By using Equation (1), a general fracture model can be expressed:

$$D\int_0^{\bar{\varepsilon}_f} f\left(\sigma,\varepsilon,\dot{\varepsilon},T,\ldots\right)\overline{d\varepsilon^p} \leq 1 \quad (1)$$

where $\bar{\varepsilon}_f$ is the equivalent strain at fracture, $\overline{d\varepsilon^p}$ is the equivalent plastic strain increment, and f is a scaling function that depends on internal variables such as stress state σ, strain rate $\dot{\varepsilon}$, and temperature T. D is seen as a damage indicator [30].

In order to accurately depict the normalized stress state, it is necessary to consider both stress triaxiality η as well as the Lode angle parameter $\bar{\theta}$. It is well-established that the strain to localization decreases when the stress triaxiality increases. Conversely, a lower stress triaxiality value results in increased sensitivity to the Lode angle parameter [244]. For isotropic materials under plane stress, the triaxiality alone is enough to define any possible stress state relevant for fracture characterization [234]. On the other hand, $\bar{\theta}$ controls the shape of a given void [31] and is required to model three-dimensional stress states.

7.1. Comparison between Different Fracture and Damage Models

This subsection presents a brief comparison regarding different types of ductile fracture and damage models, aiming to emphasize their main advantages, drawbacks, as well as application fields. For a more comprehensive overview, readers should refer to the work conducted by Cao [244] and Tekkaya et al. [31].

There is a large number of ductile fracture models. Therefore, it can be difficult to choose the most appropriate one to employ for a particular sheet metal forming process. Table 5 presents a brief and simplified qualitative comparison between the three main families of ductile fracture models.

Table 5. Qualitative comparison of the different families of ductile fracture models applied in sheet metal forming processes.

Unfavorable – 0 Favorable +		**Uncoupled Models**	**CDM Models**	**Micromechanical-Based Models**
Implementation	Simplicity	+	0	–
	Calibration	+	–	–
	Simulation Convergence	+	–	–
	CPU Time	+	–	–
Accuracy	Damage Softening	–	+	+
	NLSPs Modeling Accuracy	0	+	+
	Physical Interpretation	–	–	+
	Large Plastic Deformation Modeling	–	–	+
	Low Triaxialities Modeling Accuracy	0	–	–

For a fracture or damage model to garner acceptance within real industrial forming applications, a wise equilibrium must be attained between ease of implementation and forming behavior accuracy. In this realm, the investment time in both model formulation as well as its implementation in finite element software must be as low as possible. On the other hand, the accuracy of the model should be as high as feasible to correctly predict the component's forming behavior. Generally, these parameters work in an inverse manner.

In these contexts, phenomenological uncoupled models are commonly preferred, e.g., where components exhibit relatively straightforward geometries characterized predominantly by linear strain paths. These models are suitable for optimizing process parameters aimed at minimizing damage occurrence. The major advantage of such models consists of their ease of implementation and use. The simpler calibration procedure as well as the comparatively fewer number of parameters contribute to their quicker implementation. Additionally, since damage softening effects are not considered, mesh dependency is avoided, facilitating the simulation process: less CPU time and more convergence stability. However, it is imperative to acknowledge that the principal limitation of this category of models pertains to their applicability in scenarios involving complex loading paths outside

the identification zone, as well as those related to large plastic deformation. Thus, special care should be taken for their application outside the identification domain, due to their phenomenological foundation [244].

In many industrial applications, the loading path frequently exhibits intricate characteristics. Therefore, coupled models may be seen as an appropriate choice, since they account for the softening effect due to damage accumulation, as opposed to uncoupled models. Indeed, the coupled models' predictive damage accuracy is significantly higher. These models can capture continuous degradation due to damage. Although this is important when the material experiences very large plastic deformation in multi-step forming processes, the complexity of the simulation process is unavoidably raised, i.e., the softening effect introduces mesh dependency. As a result, finer mesh induces faster damage accumulation. In order to mitigate mesh dependency, two validated approaches can be pursued: (i) integration of non-local methodologies, which may be grounded in either integral formulations or implicit/explicit formulations, requiring careful calibration; (ii) delineation of damage model parameters tailored to specific element dimensions, ensuring that during computations, the element sizes remain beneath this predetermined threshold [31]. This mesh dependency results in an increased CPU time in comparison to uncoupled models. However, to handle the complex strain path the material may undergo, the use of phenomenological models is required [31]. No purely micro-mechanical model has been shown to be capable of capturing both damage mechanisms at high and low stress triaxialities in real multi-forming operations due to their construction and current computational efficiency [244]. Thus, micro-mechanical-based models are discarded for industrial forming process implementation. With their significantly high physical background, their complexity is high. The CPU time required as well as the calibration procedure dissuades their implementation. Conversely, CDM models require comparatively less effort in the calibration process, as a smaller number of damage parameters are used. Additionally, these models couple elasticity with damage evolution.

Therefore, each family of models has their own advantages and drawbacks. The effort one is willing to take in model accuracy, neglecting simplicity, or vice versa, is the main factor in model selection. In this context, advanced uncoupled phenomenological models are very popular in the sheet forming industry. Despite their comparatively diminished damage prediction accuracy, they have been used and demonstrated satisfactory results, even for applications involving complex stress states. Moreover, these ductile fracture models facilitate the incorporation of strain rate dependencies through accurately constructed strain-rate-dependent terms. Among all phenomenological fracture models, it is worth mentioning the modified Mohr–Coulomb (MMC) [245], the all-strain-based MMC (eMMC) [205], and the Hosford–Coulomb model (HC) [233]. All of them have shown good performance in modeling sheet metal forming fracture of AHSS representative components.

Alternatively, the adoption of 'modular' models has been progressively gaining attention. Even though coupled models generally exhibit better predictive accuracy, they encounter limitations in addressing conditions characterized by low stress triaxialities and notably shear-dominated loading conditions. Therefore, the conceptual framework of the 'modular' models is to upgrade these models by adding terms that increase predictive accuracy for specific situation (e.g., the Lode-dependent term; a strain threshold for damage accumulation that depends on stress triaxiality). When thoughtfully formulated, these diverse models may converge towards consistent predictions concerning damage location [244]. Sandin et al. [227] as well as Khameneh et al. [196] evolved the MMC model with the GISSMO model.

Table 6 provides a summary of the application of ductile fracture/damage models in selected studies from the past 15 years. Despite the research field of fracture and damage being relatively recent, sheet metal forming research has been addressing and testing the implementation of mainly phenomenological uncoupled models in representative components. Further actions may be focused on their application in real-world scenarios, to be reported within the literature.

Table 6. Summary of constitutive fracture/damage models' predictions in sheet metal forming processes of AHSS (comprising the period: 2010–2023).

Ref.	Fracture/ Damage Model	Purpose	Findings	Limitations
[228]	MMC	Employ the MMC criterion to analyze shear fracture during stretch–bending operations.	The applicability of the MMC criterion was effectively validated during stretch–bending operations.	The MMC criterion's numerical predictive accuracy is relatively dependent on the type of element selected. The shell element model's efficiency is acceptable, but its performance is not as accurate as the 3D model, particularly in predicting drawing depth, wrap angles, and wall stresses.
[101]	MMC	Assess the applicability of the MMC model to predict shear fractures, which were not effectively captured by the conventional FLC. Validate MMC predictions by accurately correlating fracture location and punch travel with experimental results for circular and square punches.	MMC accurately captured all observed features in square and cylindrical punch tests, including fracture locations, modes, and punch travels (shear fracture). Implemented MMC at all integration points through the thickness to accurately simulate crack propagation in shell elements, capturing effects not addressed by FLC.	MMC's efficacy in calibrating fracture limits for TRIP690 steel raises concerns regarding its universality across diverse materials and forming processes.
[230]	GTN	Demonstrate the capability of the GTN model to address industrial applications.	The GTN model reliably predicted the crack localization site.	Acknowledged the absence of consideration for kinematic hardening in the GTN model, which could be significant for predicting springback. Identified a limitation in the GTN model's incapacity to account for the anisotropic behavior of blank sheets during forming processes. Recognized the presence of mesh-dependent effects influencing the reliable prediction of draw depth.
[231]	CrachFEM	Compare experimental and numerical results of rectangular deep drawing of AHSS classes to assess the predictive capability of CrachFEM.	Formability assessments of CrachFEM are, in general, in correlation with the experimental outputs.	CrachFEM effectively reflects material deterioration but requires improvement for loading paths involving initial shear deformation followed by plane strain tension.
[30]	CL criterion eCL criterion JC criterion MMC	Fracture evaluation of components subjected to two test procedures: (1) Nakazima test with circular specimen; (2) two-step forming and subsequent stretching; the latter under non-linear strain path histories.	Reasonable accuracy in predicting fractures of all criteria for the Nakazima test. CL fracture criterion yields the best prediction under NLSPs.	The JC criterion predicts a slightly premature fracture displacement under the Nakazima test. The MMC and the eCL criteria should be used with care for stress triaxialities below $-1/3$.
[236]	MMC Adjusted MMC	Propose a novel adjustment to the MMC fracture model, introducing infinitely high fracture strains at strongly pressure-superimposed stress states in deep drawing processes.	The adjusted MMC model demonstrated enhanced accuracy in predicting crack initiation moments and locations during the deep drawing process.	The MMC model predicted shear fractures too early.
[222]	DSSE-HC	Introduce the DSSE concept to capture localized necking with shell element meshes, allowing for the implementation of recent progress in fracture models.	Validated the effectiveness of the DSSE-HC model for DP780 steel across various engineering applications, including hemispherical punch loading, stretch bending, and V-bending of strips.	Assumes fracture initiation in a shell element either when the loading path leaves the DSSE boundary or satisfies the HC fracture criterion. These assumptions may simplify the analysis but may not capture all nuances of real-world scenarios.
[237]	GISSMO	Calibrate the GISSMO for assessing fractures in sheet metal forming simulations.	Validated the GISSMO model on a cross-die cup scenario, demonstrating the practical applicability of the calibrated models. The location as well as the instant of onset of failure were accurately predicted.	Needs careful parameter calibration.

Table 6. *Cont.*

Ref.	Fracture/ Damage Model	Purpose	Findings	Limitations
[43]	GTN JC	Provide a numerical evaluation of the JC and GTN damage models, assessing their effectiveness in predicting damage and formability limits through Nakazima tests.	Observed that the forming limits predicted by the GTN model were generally more accurate than those obtained with the JC model.	The JC damage model predicted a smaller punch force due to material damage occurring at an earlier stage, resulting in a smaller punch stroke compared to the GTN model. Highlighted the need for further studies, including investigations into the influence of damage parameter identification and the friction model considered in numerical simulation results.
[223]	DSSE-HC	Showcase that the DSSE-HC model, when applied to shell element simulations, provides reasonable and accurate predictions for the onset of ductile failure. This includes scenarios involving both membrane- and bending-dominated loading conditions.	Demonstrated that the DSSE-HC model provides reasonable predictions of the onset of ductile failure for both membrane- and bending-dominated loading conditions.	The applicability of the HC shell model is limited to problems where the length of a neck is much smaller than the critical structural displacements.
[239]	GTN	Analyze and validate the GTN model's ability to accurately predict fracture in a hydraulic bulge test.	Numerical simulations based on the GTN model successfully predicted the fracture position and forming limit of DP500 sheets under different loading paths.	
[240]	GTN	Utilize FE simulations coupled with the GTN model to predict failure occurrences of AHHS samples in two-stage forming tests.	Demonstrated that the GTN model could fairly predict the failure states of samples undergoing different non-linear strain paths, providing a more accurate representation than the FLC criterion.	GTN parameter identification simplification led to overestimation of the critical limit strains.
[227]	MMC + GISSMO	Evaluate the accuracy of strain-driven ductile fracture models in high-strength sheet steel	Clear correlation between the FE-model results and the experimental results both in terms of force–displacement response and for predicting the bending punch stroke until failure of the bending test.	Strain-driven ductile fracture modeling of crack-tip analysis cannot be used to predict the crack initiation of cracked AHSS.
[242]	MMC	Predict shear fracture using the MMC model.	The validity of the MMC criterion is verified through stretch–bending and Nakazima tests. Established a correlation between material parameters and MMC's parameters, enabling a reduction of the amount of required experimental data, enhancing the efficiency of fracture predictions.	
[243]	HC	Utilize the HC model to simulate hole expansion deformation processes and compare the results with experimental hole expansion ratios to validate the model's effectiveness.	The model effectively captures the hole expansion deformation process in both monotonic and interrupted loading conditions, providing valuable insights into the role of stress relaxation and friction effects.	Additional investigation is necessary to determine how the damage variable evolves concerning interface friction.
[196]	MMC	Compare the predictive accuracy of the MMC model in fracture strain determination between shear and uniaxial tension by calibrating it with two different sets of experimental testing specimens: (1) Shear, Uniaxial Tension, Plane Strain Tension, and Equi-biaxial Tension; and (2) Combined Simple Shear and Uniaxial Tension.	MMC model accurately estimated fracture strain in combined Uniaxial Tension and Simple Shear. The inclusion of points corresponding to a strain path evolution between Simple Shear and Uniaxial Tension was crucial for improving calibration from Shear to Biaxial Tension.	Potential need for further validation of the MMC model across representative industrial scenarios and materials.

7.2. Phenomenological Fracture Models

In these models, fracture is assumed to occur when a critical stress or strain rate is reached. The damage variable is just a 'warning' for the approach of fracture [244]. Although most of the uncoupled models encountered in the literature have a phenomenological background, the first developed fracture models were rooted in physical principles, incorporating considerations of void growth. Examples of such models are the McClintock [246] and Rice–Tracey [247] models.

In the realm of phenomenological fracture criteria, the concept of damage is approached as an integration of a stress-based function along the loading trajectory. Initially, early research efforts solely focused on considering either stress triaxiality, e.g., the Oyane model [248], or principal stress, e.g., the Cockcroft–Latham model [171]. However, it was observed that when subjected to complex loading paths, the predictive accuracy of these models in simulating forming behavior is diminished. The primarily stems from the fact that the critical damage threshold is contingent upon the specific loading trajectory. Recognizing this limitation, Bao and Wierzbicki [249] highlighted the necessity of incorporating Lode angle parameter dependence into these criteria to establish a unique definition of the normalized stress state. Thus, the recently proposed models, named advanced uncoupled phenomenological models, comprehensively account for both stress triaxiality and Lode angle influence. These criteria usually define a fracture locus where the strain to fracture is a function of stress triaxiality and Lode angle [31]. Nevertheless, it is prudent to acknowledge that while such models enhance predictive accuracy within complex stress states, further refinements are necessary to address non-linear strain paths. In such cases, the equivalent strain to fracture no longer represents the actual strain at fracture but rather serves as a weighting function that accounts for the stress state [244].

7.2.1. Modified Mohr–Coulomb Model (MMC)

The Modified Mohr–Coulomb model [204] was proposed by Bai and Wierzbicki. The model was formulated by the transformation of the stress-based Mohr–Coulomb (MC) criterion to the corresponding strain-based model, where the spherical coordinate system is derived in terms of $\overline{\varepsilon_f}$, η, and $\bar{\theta}$. The damage indicator can be formulated as in Equation (5), where $\bar{\varepsilon}_p$ represents the equivalent plastic strain:

$$D\left(\bar{\varepsilon}_f\right) = \int_0^{\bar{\varepsilon}_p} \frac{\overline{d\varepsilon^p}}{f\left(\eta, \bar{\theta}\right)} \tag{2}$$

The fracture locus is calculated according to:

$$\overline{\varepsilon_f} = \left\{ \frac{A}{c_2}\left[c_\theta^S + \frac{\sqrt{3}}{2-\sqrt{3}}\left(c_\theta^{ax} - c_\theta^S\right)\left(\sec\left(\frac{\theta\pi}{6}\right) - 1\right)\right]\left[\sqrt{\frac{1+c_1^2}{3}}.\cos\left(\frac{\theta\pi}{6}\right) + c_1\left(\eta + \frac{1}{3}sen\left(\frac{\theta\pi}{6}\right)\right)\right]\right\}^{\frac{-1}{n}} \tag{3}$$

There are a total of six parameters (A, n, c_1, c_2, c_θ^s, c_θ^c) that need to be determined. Parameter A and n represent the Swift hardening law parameters, while the remaining parameters are material constants. These constants are determined through a minimum of three fracture experimental tests conducted at different stress triaxiality ranges.

The engineering applicability of the MMC fracture model for TRIP690 steel was demonstrated by Li et al. [101]. They accurately predicted the fracture location and magnitude of punch travel for two deep-drawing operation setups: square punch and circular punch. Furthermore, the results indicated that the MMC model outperformed the FLC criterion in dealing with NLSPs and shear-induced fracture. Nevertheless, Behrens et al. [236] highlighted the significance of considering no damage accumulation effects for stress triaxialities below −0.33 in the MMC formulation. Their study detected premature shear fracture initiation of a DP600 steel workpiece in a deep drawing operation without the aforementioned condition. Luo and Wierzbicki [228] investigated the accuracy of the MMC

model in predicting fracture behavior in stretch forming simulator tests. The comparative evaluation between different element types revealed that both 3D and shell elements are sufficiently adequate to fit the experimental fracture data. The fracture location/mode, fracture wall stress, and fracture wrap angle are particularly well-predicted by the 3D element type. Moreover, the MMC model can detect variations in experimental friction conditions. More recently, Fu et al. [242] also proved the effectiveness of the MMC model for predicting ductile fracture both in stretch–bending and Nakazima tests for DP980 and DP1180 steels.

7.2.2. Strain Based Modified Mohr–Coulomb (eMMC)

The eMMC model is derived by converting the stress state variables η and $\bar{\theta}$ from the MMC model to the strain state. By considering the stress ratio β and the strain ratio α of in-plane principal strain increments, the model can be expressed in a space based solely on strain. In this space, the fracture strain is affected by either the strain ratio or a new plastic strain based parameter, ϕ [205]:

$$\alpha = \frac{d\varepsilon_2}{d\varepsilon_1},\ \beta = \frac{\sigma_2}{\sigma_1} \tag{4}$$

The eMMC formulation is based on the premise of monotonic loading and the plastic flow rule of Mises–Levy. This formulation enables the establishment of a correlation between α and β:

$$\alpha = \frac{2\beta - 1}{2 - \beta},\ \beta = \frac{2\alpha + 1}{2 + \alpha} \tag{5}$$

One significant benefit of transforming the MMC into the eMMC lies in the decoupling of the fracture model from plasticity, allowing for the study of fractures independent of plasticity [205]. This is achieved by the introduction of the ϕ parameter, denoted as:

$$\phi = \frac{180^\circ}{\pi} atan2\left(-\dot{\varepsilon}_2^p, -\dot{\varepsilon}_1^p\right) + 90^\circ \tag{6}$$

The ϕ parameter represents the effect of in-plane anisotropy under all possible loading conditions. Furthermore, it denotes the angle to the positive minor strain direction in the forming fracture limit diagram (FFLD) under proportional loading.

A calibration study conducted by Jia and Bai [205] demonstrated good accuracy in predicting the eMMC fracture locus for TRIP780 steel. Their study combined experimental and numerical methods and produced precise estimates for material strength, plastic flow behavior, fracture initiation location, and fracture propagation modes.

7.2.3. Hosford–Coulomb (HC)

Mohr and Marcadet [233] proposed the Hosford–Coulomb phenomenological model, which is motivated by micromechanics and assumes that fracture onset is closely linked to the formation of a primary or secondary band of localization. Despite being a phenomenological model, the underlying physical significance of the stress-based localization criteria is preserved. The HC model converts the stress space of the localization criterion into a mixed strain–stress space, incorporating the equivalent plastic strain, stress triaxiality, and Lode angle parameter. The HC model was specifically developed by Mohr and Marcadet to cater to the distinctive characteristics of AHSS. The accuracy of the model was confirmed by these authors under proportional loading and at low strain rates for three AHSS materials (DP590, DP780, TRIP780).

According to the HC model, fracture occurs when the following conditions are met:

$$\int_0^{\bar{\varepsilon}_f} \frac{d\bar{\varepsilon}_p}{\bar{\varepsilon}_f^{pr}\left[\eta, \bar{\theta}\right]} = 1 \tag{7}$$

where $\bar{\varepsilon}_f^{pr}$ represents the equivalent plastic strain at the onset of fracture for proportional loading. In the mixed strain space, the criterion is defined as in Equation (11):

$$\bar{\varepsilon}_f^{pr} = k^{-1}\left[\sigma_f\left[\eta\bar{\theta}\right]\right] \tag{8}$$

In the Modified Haigh–Westergaard stress space, $\bar{\sigma}$ takes the form of:

$$\bar{\sigma} = \bar{\sigma}_f[\eta,\bar{\theta}] = \frac{b}{\left\{\frac{1}{2}\left((f_1-f_2)^a + (f_2-f_3)^b + (f_1-f_3)^a\right)\right\}^{\frac{1}{a}} + c(2\eta + f_1 + f_3)} \tag{9}$$

The model parameters are referred as a, b, and c.

Compared to the MC criterion, the HC model exhibits greater suitability for handling biaxial loading [233]. Roth and Mohr [232] proposed an empirical extension to the HC model, which considers the influence of strain rate on fracture initiation in two AHSS materials (DP590 and TRIP780). This extension introduces an additional scalar parameter to the model formulation to account for strain rate effects. A similar approach was adopted by Erice et al. [226], who verified that the HC model provides a satisfactory approximation of the impact of stress triaxiality and Lode angle parameter on three other AHSS (DP980, CP980 and CP1180).

The calibration procedure of the aforementioned studies was addressed through numerical simulations using solid elements. However, when it comes to calibrating the HC using shell elements, it becomes necessary to establish the Domain of Shell-to-Solid Equivalence (DSSE) in order to achieve convergence in the initiation of ductile fracture relative to the mesh size [223]. To address this issue, Pack and Mohr [222] introduced the DSSE-HC model, which combines the DSSE concept with the Hosford–Coulomb model. The DSSSE-HC model can capture fracture initiation without prior necking, as well as through-thickness necking failure. Notably, the DSSE approach offers the advantage of distinguishing between membrane and bending loading conditions, setting it apart from the FLD/FLC criterion. Fracture is assumed to occur when the loading path in a shell element either departs from the DSSE boundary or satisfies the HC fracture criterion. The DSSE-HC model was successfully calibrated for DP780 steel and was applied to accurately predict the displacement to fracture in both stretch bending and 'V-bending' operations. However, as highlighted by Pack et al. [223], further enhancements are necessary to mitigate the pronounced mesh size dependence of fracture predictions when employing a combined ductile fracture model and a necking-based forming limit criterion.

Furthermore, the efficacy of the HC model in investigating the impact of interrupted loading conditions, as often encountered in servo press forming operations, has been demonstrated by Prasad et al. [243].

7.3. Continuum Damage Models (CDMs)

CDM models are classified as phenomenological due to their foundational development hinging upon a rigorous thermodynamic framework, thereby ensuring non-negative dissipation [244]. The degradation of material stiffness is addressed through the introduction of an internal scalar damage variable, which interacts with the stress tensor to account for isotropic damage phenomena. To impart the macroscopic response with damage effects, the concept of effective stress is introduced based on the principle of strain equivalence. This notion of effective stress allows for a unified integration of damage evolution with the material behavior law, enabling the consideration of damage effects on both elasticity and plasticity [31].

The first contributor towards the formulation of models grounded in thermodynamical assumptions was Kachanov [250]. Subsequent improvements in this theoretical domain were introduced by Chaboche [251] and Lemaitre [252]. Indeed, among CDM models, the Lemaitre damage model is widely used, wherein stress triaxiality and equivalent stress are the pivotal factors governing damage propagation. Notably, Lemaitre's model underwent enhancements, aiming to tailor their applicability to metal forming applications. These adaptations encompassed the augmentation of the damage dissipation potential, with

Lemaitre and Desmorat [253] introducing a strain threshold beyond which damage remain constant [31]. To further enhance model accuracy, particularly at low stress triaxialities, Cao et al. [254] devised the Lemaitre Enhanced Model (LEL) by including a parabolic Lode-dependent term. The main modifications focused on [244]: (i) accounting for the influence of the Lode Angle parameter on damage evolution; (ii) improving the influence of stress triaxiality on the damage threshold; (iii) enhancing the weakening function at low stress triaxialities.

Another notable CDM model is the Generalized Incremental Stress State-Dependent Damage Model (GISSMO) [234]. In this model, in addition to the damage variable D, an instability function F dependent on the critical strain $\varepsilon_{crit}(\eta)$ is introduced. Once F reaches 1, the coupling between damage and the stress tensor is activated [31].

GISSMO Model

Neukamm et al. [255] initially formulated GISSMO, which was later enhanced to incorporate Lode angle dependency by Basaran et al. [256]. Additional details about the GISSMO model were provided by Andrade et al. [234]. GISSMO is a phenomenological damage model that uses stress state-dependent equivalent plastic strain as fracture criteria [227]. It is uncoupled from the plasticity model. The GISSMO model is implemented in the commercial finite element code *LS-DYNA*.

The incorporation of a damage accumulative parameter, which is dependent on the plastic strain increment, allows for the accurate modeling of non-proportional loading histories. In this context, the damage variable, with respect to time, is provided by Equation (13):

$$\dot{D} = \frac{n}{\varepsilon_f(\eta)}.D^{(1-\frac{1}{n})}.\dot{\varepsilon}_p \tag{10}$$

This expression serves as an evolutionary equation that effectively addresses non-proportional loading histories. Additionally, the authors have introduced an instability function, denoted as F, capable of understanding when strain localization arises, and therefore accelerating material degradation when those situations occur. Using this approach, the eventual non-linearity affecting the onset fracture behavior is taken into consideration. To deal with mesh dependency, a triaxiality-dependent regularization strategy is adopted, adjusting the fracture curve to the corresponding element size.

One of the main advantages of the GISSMO model lies in its ease of numerical implementation in comparison to other CDM models. Its feature of allowing coupling with any plastic material model ensures high flexibility. The resulting curves from the GISSMO model are presented in Figure 18. The calibration procedure involves the determination of several parameters, including the fracture curve as a function of stress triaxiality, $\varepsilon_f(\eta)$, the damage exponent, n, the curve for critical strain, $\varepsilon_{crit.}(\eta)$, and the fading exponent, m.

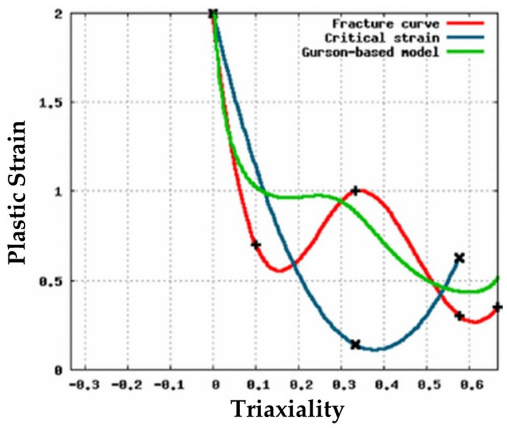

Figure 18. Ductile-calibrated fracture and critical plastic strain curves for the GISSMO model. Reprinted from Ref. [234] with permission. Copyright 2015, Springer Link.

7.4. Micro-Mechanics-Based Models

Micro-mechanics-based models consider the underlying physical meaning attributed to the damage. Hence, the macroscopic feature is a result of the micro-mechanical void, void growth, and the coalescence of neighboring voids. Material deterioration is linked with fracture occurrence. Micro-mechanics-based models can be subdivided into: (i) Gurson-like approach, (ii) non-linear homogenization-based approach.

The effect of void growth on material degradation was introduced by Gurson [257]. The widely recognized Gurson–Tvergaard–Needleman (GTN) model [258] represents a further advancement of the Gurson framework. The GTN is a porous plasticity theory, accounting for the evolution of the void volume fraction, interaction, nucleation, and final coalescence of voids, where the void growth depends on the trace of the plastic strain rate [31]. Multiple extensions have been proposed to enhance the GTN model's accuracy, exemplified by the development of the GLD model, which accounts for void shape effects. Stress triaxiality and Lode angle-dependent terms can be integrated into these models. As the main drawback of the micro-mechanics-based models, particularly the GTN model, is the low accuracy in predicting shear-dominated loading cases, the incorporation of these stress state parameters increases the model's accuracy. Stress triaxiality allows the void nucleation process to take place earlier at high stress triaxialities [244]. Xue [259] and Nahshon and Hutchinson [260] added a Lode-dependent term to more accurately model the void growth [31]. However, these modifications are purely phenomenological.

The non-linear homogenization-based approach models can describe the changes in void shape and orientation, which have been shown to be important at low stress triaxialities [244].

Gurson–Tvergaard–Needleman (GTN) Model

The GTN model postulates that damage growth is an outcome of material degradation, occurring as the loading process takes place. Void evolution plays a crucial role in shaping the yielding behavior and is appropriately incorporated into the GTN model through a modification of the Von Mises yield potential [261]:

$$\phi = \left(\frac{\sigma_v}{\sigma_Y}\right)^2 + 2q_1 f^* \cosh\left(\frac{3}{2} q_2 \frac{\sigma_H}{\sigma_Y}\right) - \left(1 + q_3 f^{*2}\right) = 0 \tag{11}$$

where σ_v represents the Von Mises equivalent stress, σ_Y denotes the matrix material yield stress, and σ_H refers to the hydrostatic component. q_1, q_2, and q_3 are material constants. f^* represents the effective volume void fraction, capturing the effects of void coalescence.

The evolution of voids is mathematically defined as follows:

$$\dot{f} = \dot{f}_{growth} + \dot{f}_{nucleation} \tag{12}$$

where $\dot{f}_{growth}$ and $\dot{f}_{nucleation}$ are determined through Equations (13) and (14):

$$\dot{f}_{growth} = (1 - f)\dot{\varepsilon}^{pl}_{kk} \tag{13}$$

$$\dot{f}_{nucleation} = \frac{f_N}{S_N\sqrt{2\pi}} \dot{\bar{\varepsilon}}_p e^{\left(-\frac{1}{2}\frac{\bar{\varepsilon}_p - \varepsilon_N}{S_N}\right)^2} \tag{14}$$

The volume dilatation rate is denoted by $\dot{\varepsilon}^{pl}_{kk}$, whereas $\bar{\varepsilon}^{pl}$ represents the equivalent plastic strain, and $\dot{\bar{\varepsilon}}^{pl}$ is the rate of the equivalent plastic strain. The standard deviation is represented by S_N.

The effective volume void fraction f^* accounts for the micro-mechanics at work, including the presence of micro-voids, the growth of voids, and the coalescence of neigh-

boring voids leading up to fracture at the macroscopic level [147]. f^* is determined, as per Equation (15):

$$f^*(f) = \begin{Bmatrix} f \\ f_C + K(f - f_C) \end{Bmatrix} \begin{matrix} f \leq f_C \\ f > f_C \end{matrix} \quad (15)$$

where $K = \frac{f^*_{u-f_C}}{f_f - f_C}$.

In this context, the void volume fraction, critical void volume fraction, and void volume fraction at macroscopic failure are denoted by f, f_c, and f_f, respectively. The modified void volume fraction at macroscopic failure is represented by $f^*_u = f^*(f_f)$. The calibration process for the GTN model requires determination of a total of eight parameters, where a few parameters can be found in the existing literature (q_1, q_2, and S_N) [230]. Moreover, f_f is frequently assumed to be 10% [262]. In the study conducted by Cui et al. [239], f_f was computed through observations of the fracture morphology using SEM technology. Employing response surface methodology, five other parameters (f_0, f_N, f_c, ε_N, S_N) were determined. In addition, Achineethongkham and Uthaisangsuk [240] identified damage model parameters through the use of metallographic analyses, local strain measurement, and representative volume element (RVE) simulations.

The analysis of local crack initiation in Nakazima forming process on DP600 and TRIP600 steel was carried out by Uthaisangsuk et al. [261] through the application of the GTN damage model. Their findings indicated that this microstructure-based damage model provided satisfactory predictions of the fracture behavior of both multiphase steels in Nakazima stretching tests. Nevertheless, the influence of stress triaxiality on the fracture behavior has to be taken into account due to the void formation mechanism, which might be described by modifying model parameters [261]. Doig and Roll [230] stated that the GTN model is appropriate to treat real industrial cases. In their study, the GTN model accurately predicted the localization of cracks in a cross-die part. However, similar to the FLD criterion, the coupled model overestimated the drawing depth, as opposed to the work conducted by Cui et al. [239], who observed that the fracture position and limit strains in various loading conditions of a bulge test were almost identical between experimental and numerical simulation results of DP590 steel. Furthermore, the GTN model was employed for evaluating the forming behavior in two-stage forming processes, as concluded by Achineethongkham et al. [240]. The authors concluded that the GTN model provided reliable predictions for the fracture states of samples subjected to NLSPs.

8. Conclusions

The shift towards the employment of AHSS in BiW components has been leading to forming challenges almost never encountered when forming conventional mild steels. Shear cracks, edge cracks, and surface cracks are more frequently noticed within sheet metal forming industrial operations. The conventional FLD is unable to accurately model and account for these fracture occurrences.

The state-of-the-art presented in this paper addresses the current trends to improve the forming behavior and fracture modeling accuracy of sheet metal forming processes. The FLD's limitations and main drawbacks dealing with fracture occurrences are analyzed, as well as the academic directions followed to overcome those limitations. The Generalized Forming Limit Curve (GFLC) is an upgrade to the conventional FLD, currently implemented in AutoForm R10, aiming to improve accuracy in modeling non-linear strain paths. However, further enhancements are required to deal with fracture modeling. Material modeling is significant for forming behavior accuracy. Thus, a comprehensive review of material modeling is provided. The directions followed by the academic community with respect to material characterization methods and techniques are presented. Further improvements, particularly for pure shear stress states, are required in order to develop standardized specimens. Furthermore, damage and fracture models are subjected to analysis.

Formability evaluation should be attained by analyzing failure on account of through-thickness necks and splits as well as direct fracture. The consideration of a central frame-

work is necessary to account for all relevant phenomenological outcomes. In this context, advanced uncoupled phenomenological models are a promising approach. In order to garner industrial acceptance, simplicity of use and implementation are favored. The Generalized Incremental Stress State-Dependent-Damage Model (GISSMO), as well as 'modular' models, have also been shown to provide accurate results. However, the analysis of relevant case studies, covering a wide range of stress states and complex strain paths, is required to further enhance fracture modeling accuracy of such models when applied to AHSS in real industrial applications.

Funding: This research was funded by Fundação para a Ciência e a Tecnologia (FCT), grant number 2022.13884.BDANA.

Data Availability Statement: Not applicable.

Conflicts of Interest: Author Sérgio L. Costa was employed by the company Bairrimoldes Lda. The remaining authors declare that the research was conducted in the absence of any commercial or financial relationships that could be construed as a potential conflict of interest.

References

1. European Environment Agency. *Trends and Projections in Europe 2023*; Publications Office: Luxembourg, 2023.
2. Environmental Issues Facing Future of European Car Industry Marketing Essay. Available online: https://www.ukessays.com/essays/marketing/environmental-issues-facing-future-of-european-car-industry-marketing-essay.php (accessed on 23 March 2023).
3. Kelly, J.C.; Sullivan, J.L.; Burnham, A.; Elgowainy, A. Impacts of Vehicle Weight Reduction via Material Substitution on Life-Cycle Greenhouse Gas Emissions. *Environ. Sci. Technol.* **2015**, *49*, 12535–12542. [CrossRef] [PubMed]
4. Zhang, W.; Xu, J. Advanced Lightweight Materials for Automobiles: A Review. *Mater. Des.* **2022**, *221*, 110994. [CrossRef]
5. Giampieri, A.; Ling-Chin, J.; Ma, Z.; Smallbone, A.; Roskilly, A.P. A Review of the Current Automotive Manufacturing Practice from an Energy Perspective. *Appl. Energy* **2020**, *261*, 114074. [CrossRef]
6. Tisza, M.; Czinege, I. Comparative Study of the Application of Steels and Aluminium in Lightweight Production of Automotive Parts. *Int. J. Lightweight Mater. Manuf.* **2018**, *1*, 229–238. [CrossRef]
7. Trzepieciński, T.; Najm, S.M. Current Trends in Metallic Materials for Body Panels and Structural Members Used in the Automotive Industry. *Materials* **2024**, *17*, 590. [CrossRef]
8. Khedkar, P.; Motagi, R.; Mahajan, P.; Makwana, G. A Review on Advance High Strength Steels. *Int. J. Curr. Eng.* **2016**, *6*, 240–243.
9. Schmitt, J.-H.; Iung, T. New Developments of Advanced High-Strength Steels for Automotive Applications. *Comptes Rendus Phys.* **2018**, *19*, 641–656. [CrossRef]
10. Kuziak, R.; Kawalla, R.; Waengler, S. Advanced High Strength Steels for Automotive Industry. *Arch. Civ. Mech. Eng.* **2008**, *8*, 103–117. [CrossRef]
11. Banana Diagram Archives. Available online: https://ahssinsights.org/tag/banana-diagram/ (accessed on 12 February 2024).
12. WorldAutoSteel. Available online: https://www.worldautosteel.org/ (accessed on 12 February 2024).
13. Marretta, L. Sheet Stamping Processes Design: Optimization Methodologies for Robust and Environmental Conscious Decisions. Ph.D. Thesis, Università Degli Studi di Palermo, Palermo, Italy, 2011.
14. A Meaningful Review of Metal Stamping and Safety. MCR Safety Info Blog. Available online: https://www.mcrsafety.com/en/blog/2019/august/metal-stamping (accessed on 23 March 2023).
15. Fekete, J.R. Manufacturing Challenges in Stamping and Fabrication of Components from Advanced High Strength Steel. In Proceedings of the International Symposium on Niobium Microalloyed Sheet Steel for Automotive Applications, Araxa, Brazil, 5–8 December 2005; pp. 107–115.
16. Gomes, T.; Silva, F.J.G.; Campilho, R.D.G.S. Reducing the Simulation Cost on Dual-Phase Steel Stamping Process. *Procedia Manuf.* **2017**, *11*, 474–481. [CrossRef]
17. Lee, E.-M.; Shim, D.-S.; Son, J.-Y.; Baek, G.-Y.; Yoon, H.-S.; Ro, K.-B. Study on Design of Progressive Dies for Manufacture of Automobile Structural Member Using DP980 Advanced High Strength Steel. *J. Mech. Sci. Technol.* **2016**, *30*, 853–864. [CrossRef]
18. Shawn Cheng, H.; Cao, J.; Xia, Z.C. An Accelerated Springback Compensation Method. *Int. J. Mech. Sci.* **2007**, *49*, 267–279. [CrossRef]
19. Gan, W.; Wagoner, R.H. Die Design Method for Sheet Springback. *Int. J. Mech. Sci.* **2004**, *46*, 1097–1113. [CrossRef]
20. Jiao-Jiao, C.; Jian-Guo, C.; Qiu-Fang, Z.; Jiang, L.; Ning, Y.; Rong-guo, Z. A Novel Approach to Springback Control of High-Strength Steel in Cold Roll Forming. *Int. J. Adv. Manuf. Technol.* **2020**, *107*, 1793–1804. [CrossRef]
21. Manopulo, N.; Carleer, B. On the Way towards a Comprehensive Failure Modelling for Industrial Sheet Metal Stamping Processes. *IOP Conf. Ser. Mater. Sci. Eng.* **2019**, *651*, 012004. [CrossRef]
22. Billur, E. Challenges in Forming Advanced High Strength Steels. In Proceedings of the New Developments in Sheet Metal Forming, Toyohashi, Japan, 19–22 September 2010.

23. Hu, Q.; Zhang, F.; Li, X.; Chen, J. Overview on the Prediction Models for Sheet Metal Forming Failure: Necking and Ductile Fracture. *Acta Mech. Solida Sin.* **2018**, *31*, 259–289. [CrossRef]
24. Lakkannavar, V.; Kattimani, K. Modelling and Failure Analysis In Sheet Metal Forming Process Using Cae. *Int. J. Eng. Res. Technol.* **2014**, *3*, 1422–1425.
25. Complex Phase (CP) Steels for the Highest Hole Expansion Ratios. Available online: https://www.ssab.com/en/brands-and-products/docol/automotive-steel-grades/complex-phase-steel (accessed on 4 April 2023).
26. Dual Phase (DP) Steel: Excellent Ductility and Energy Absorption. Available online: https://www.ssab.com/en/brands-and-products/docol/automotive-steel-grades/dual-phase-steel (accessed on 4 April 2023).
27. Martensitic Steel: Excellent Formability-to-Strength Ratio. Available online: https://www.ssab.com/en/brands-and-products/docol/automotive-steel-grades/martensitic-steel (accessed on 4 April 2023).
28. TRIP Steels. Available online: https://automotive.arcelormittal.com/products/flat/first_gen_AHSS/TRIP (accessed on 4 April 2023).
29. Peixinho, N.; Jones, N.; Pinho, A. Application of Dual-Phase and TRIP Steels on the Improvement of Crashworthy Structures. In *Materials Science Forum*; Trans Tech Publications Ltd.: Stafa, Switzerland, 2005; Volume 502, pp. 181–188, ISBN 978-0-87849-980-9.
30. Björklund, O.; Govik, A.; Nilsson, L. Prediction of Fracture in a Dual-Phase Steel Subjected to Non-Linear Straining. *J. Mater. Process. Technol.* **2014**, *214*, 2748–2758. [CrossRef]
31. Tekkaya, A.E.; Bouchard, P.-O.; Bruschi, S.; Tasan, C.C. Damage in Metal Forming. *CIRP Ann.* **2020**, *69*, 600–623. [CrossRef]
32. Sivam, S.P.S.S.; Saravanan, K.; Pradeep, N.; Jain, A.S.; Sekar, S.G.; Vishaal, N.A.N.D.A.M. Overview and assessment of formability effect of material properties of sheet metal—A short communication. *J. Ind. Pollut. Control* **2017**, *33*, 1732–1738.
33. Mattiasson, K.; Jergéus, J.; DuBois, P. On the Prediction of Failure in Metal Sheets with Special Reference to Strain Path Dependence. *Int. J. Mech. Sci.* **2014**, *88*, 175–191. [CrossRef]
34. Hou, B.; Huang, Y.; Ding, M.; Dong, H. Effect of Temperature and Strain Rate Fluctuation on Forming Limit Curve of 5083 Al-Mg Alloy Sheet. *Adv. Mech. Eng.* **2022**, *14*, 168781322211074. [CrossRef]
35. Sattarpanah Karganroudi, S.; Shojaei, S.; Hashemi, R.; Rahmatabadi, D.; Jamalian, S.; Aminzadeh, A.; Ibrahim, H. Insight into the Influence of Punch Velocity and Thickness on Forming Limit Diagrams of AA 6061 Sheets—Numerical and Experimental Analyses. *Metals* **2021**, *11*, 2010. [CrossRef]
36. Kasaei, M.M.; Oliveira, M.C. Influence of the Contact with Friction on the Deformation Behavior of Advanced High Strength Steels in the Nakajima Test. *J. Strain Anal. Eng. Des.* **2022**, *57*, 193–207. [CrossRef]
37. Wang, H.; Wang, Z. Theoretical Forming Limit Diagram Based on Induced Stress in the Thickness Direction. *Metals* **2023**, *13*, 456. [CrossRef]
38. Hussein, T.; Umar, M.; Qayyum, F.; Guk, S.; Prahl, U. Micromechanical Effect of Martensite Attributes on Forming Limits of Dual-Phase Steels Investigated by Crystal Plasticity-Based Numerical Simulations. *Crystals* **2022**, *12*, 155. [CrossRef]
39. Liu, R.; Sun, L.; Wang, X.; Lin, L.; Zhang, L.; Lin, J. Strain Rate Effect on Forming Limit Diagram for Advanced High Strength Steels. *SAE Int. J. Mater. Manf.* **2014**, *7*, 583–587. [CrossRef]
40. 14:00–17:00 ISO 12004-2:2008. Available online: https://www.iso.org/standard/43621.html (accessed on 23 March 2023).
41. Nakazima, K.; Kikuma, T.; Hasuka, K. *Study on the Formability of Steel Sheets*; Technical Research Institute of Yawata Works: Yawata, Japan, 1968; pp. 8517–8530.
42. Marciniak, Z.; Kuczyński, K. Limit Strains in the Processes of Stretch-Forming Sheet Metal. *Int. J. Mech. Sci.* **1967**, *9*, 609–620. [CrossRef]
43. Amaral, R.; Santos, A.D.; José, C.d.S.; Miranda, S. Formability Prediction for AHSS Materials Using Damage Models. *J. Phys. Conf. Ser.* **2017**, *843*, 012018. [CrossRef]
44. Bergs, T.; Nick, M.; Trauth, D.; Klocke, F. Damage Evolution in Nakajima Tests of DP800 Dual Phase Steel. *IOP Conf. Ser. Mater. Sci. Eng.* **2018**, *418*, 012048. [CrossRef]
45. Novák, V.; Valeš, M.; Tatíček, F.; Šanovec, J.; Chrášťanský, L. The Effect of Strain Rate on Position of Forming Limit Curve. In Proceedings of the METAL 2019—28th International Conference on Metallurgy and Materials, Brno, Czech Republic, 22–24 May 2019; pp. 450–454.
46. Ribas, L.M.; Gipiela, M.L.; Lajarin, S.F.; Filho, R.A.C.; Marcondes, P.V.P. Comparative Study of Six Failure Criteria via Numerical Simulation of Stamped DP600 Steel. *Int. J. Adv. Manuf. Technol.* **2022**, *121*, 2427–2435. [CrossRef]
47. Champolivier, E.; Brancherie, D.; Feissel, P.; Gaied, S.; Canourgues, J.-F. Experimental Characterization of Forming Behavior of 3rd GEN AHSS. *IOP Conf. Ser. Mater. Sci. Eng.* **2023**, *1284*, 012077. [CrossRef]
48. Cui, H.; Li, D.; Fu, Q.; Lu, Z.; Xu, J.; Jiang, N. Research on Forming Limit Stress Diagram of Advanced High Strength Dual-Phase Steel Sheets. *Materials* **2023**, *16*, 4543. [CrossRef] [PubMed]
49. Rahmatabadi, D.; Hashemi, R.; Tayyebi, M.; Bayati, A. Investigation of Mechanical Properties, Formability, and Anisotropy of Dual Phase Mg–7Li–1Zn. *Mater. Res. Express* **2019**, *6*, 096543. [CrossRef]
50. Rahmatabadi, D.; Tayyebi, M.; Najafizadeh, N.; Hashemi, R.; Rajabi, M. The Influence of Post-Annealing and Ultrasonic Vibration on the Formability of Multilayered Al5052/MgAZ31B Composite. *Mater. Sci. Technol.* **2021**, *37*, 78–85. [CrossRef]
51. Shao, Z.; Bai, Q.; Li, N.; Lin, J.; Shi, Z.; Stanton, M.; Watson, D.; Dean, T. Experimental Investigation of Forming Limit Curves and Deformation Features in Warm Forming of an Aluminium Alloy. *Proc. Inst. Mech. Eng. Part B J. Eng. Manuf.* **2018**, *232*, 465–474. [CrossRef]

52. Paul, S.K. Controlling Factors of Forming Limit Curve: A Review. *Adv. Ind. Manuf. Eng.* **2021**, *2*, 100033. [CrossRef]
53. Hou, Y.; Myung, D.; Park, J.K.; Min, J.; Lee, H.-R.; El-Aty, A.A.; Lee, M.-G. A Review of Characterization and Modelling Approaches for Sheet Metal Forming of Lightweight Metallic Materials. *Materials* **2023**, *16*, 836. [CrossRef] [PubMed]
54. Kumar, S.D.; Amjith, T.R.; Anjaneyulu, C. Forming Limit Diagram Generation of Aluminum Alloy AA2014 Using Nakazima Test Simulation Tool. *Procedia Technol.* **2016**, *24*, 386–393. [CrossRef]
55. Martínez-Donaire, A.; Vallellano, C.; Morales-Palma, D.; García-Lomas, F.J. Experimental Detection of Necking in Stretch-Bending Conditions: A Critical Review and New Methodology. *Steel Res. Int.* **2010**, *81*, 785–788.
56. Zhang, L.; Lin, J.; Sun, L.; Wang, C.; Wang, L. A New Method for Determination of Forming Limit Diagram Based on Digital Image Correlation. *SAE Technical Paper*, 8 April 2013; pp. 2013–01–1421.
57. Merklein, M.; Kuppert, A.; Geiger, M. Time Dependent Determination of Forming Limit Diagrams. *CIRP Ann.* **2010**, *59*, 295–298. [CrossRef]
58. Iquilio, R.A.; Cerda, F.M.C.; Monsalve, A.; Guzmán, C.F.; Yanez, S.J.; Pina, J.C.; Vercruysse, F.; Petrov, R.H.; Saavedra, E.I. Novel Experimental Method to Determine the Limit Strain by Means of Thickness Variation. *Int. J. Mech. Sci.* **2019**, *153*, 208–218. [CrossRef]
59. Huang, L.; Shi, M. Determination of the Forming Limit Curve Using Digital Image Correlation—Comparison of Different Approaches to Pinpoint the Onset of Localized Necking. *SAE Technical Paper*, 28 March 2017; pp. 2017–01–0301.
60. Volk, W.; Hora, P. New Algorithm for a Robust User-Independent Evaluation of Beginning Instability for the Experimental FLC Determination. *Int. J. Mater. Form.* **2011**, *4*, 339–346. [CrossRef]
61. Hotz, W.; Merklein, M.; Kuppert, A.; Friebe, H.; Klein, M. Time Dependent FLC Determination Comparison of Different Algorithms to Detect the Onset of Unstable Necking before Fracture. *KEM* **2013**, *549*, 397–404. [CrossRef]
62. Min, J.; Stoughton, T.B.; Carsley, J.E.; Lin, J. A Method of Detecting the Onset of Localized Necking Based on Surface Geometry Measurements. *Exp. Mech.* **2017**, *57*, 521–535. [CrossRef]
63. Martínez-Donaire, A.J.; García-Lomas, F.J.; Vallellano, C. New Approaches to Detect the Onset of Localised Necking in Sheets under Through-Thickness Strain Gradients. *Mater. Des.* **2014**, *57*, 135–145. [CrossRef]
64. Ozturk, F.; Dilmec, M.; Turkoz, M.; Ece, R.E.; Halkaci, H.S. Grid Marking and Measurement Methods for Sheet Metal Formability. In Proceedings of the 5th International Conference and Exhibition on Design and Production of Machines and Dies/Molds, Kusadasi, Turkey, 18 June 2009; pp. 41–49.
65. Mäntyjärvi, K.; Tulonen, J.; Saarnivuo, T.; Porter, J.; Karjalainen, J.A. Grid Patterns by Laser for Forming Strain Analysis. *Int. J. Mater. Form.* **2008**, *1*, 249–252. [CrossRef]
66. Guk, S.; Preiß, M.; Kawalla, R. Metal Formability Interactions in Laser Marking for Creating of Grid Patterns for Forming Strain Analysis of High Strength Steels. *KEM* **2017**, *746*, 92–98. [CrossRef]
67. Yildiz, R.A.; Yilmaz, S. The Verification of Strains Obtained by Grid Measurements Using Digital Image Processing for Sheet Metal Formability. *J. Strain Anal. Eng. Des.* **2017**, *52*, 506–514. [CrossRef]
68. Li, D.C.; Liang, J.; Hu, H.; Tang, Z.Z.; Guo, X.; Li, L.G. Strain Measurement for Sheet Metal Forming Based on Close Range Photogrammetry. *AMM* **2013**, *475*, 148–155. [CrossRef]
69. Wankhede, P.; Suresh, K. A Review on the Evaluation of Formability in Sheet Metal Forming. *Adv. Mater. Process. Technol.* **2020**, *6*, 458–485. [CrossRef]
70. Li, H.; Li, G.; Gao, G.; Zhang, W.; Wu, X. A Formability Evaluation Method for Sheet Metal Forming with Non-Linear Strain Path Change. *Int. J. Mater. Form.* **2018**, *11*, 199–211. [CrossRef]
71. Bandyopadhyay, K.; Basak, S.; Panda, S.K.; Saha, P. Use of Stress Based Forming Limit Diagram to Predict Formability in Two-Stage Forming of Tailor Welded Blanks. *Mater. Des.* **2015**, *67*, 558–570. [CrossRef]
72. Sajun Prasad, K.; Panda, S.K.; Kar, S.K.; Sen, M.; Murty, S.V.S.N.; Sharma, S.C. Microstructures, Forming Limit and Failure Analyses of Inconel 718 Sheets for Fabrication of Aerospace Components. *J. Mater. Eng. Perform.* **2017**, *26*, 1513–1530. [CrossRef]
73. Wankhede, P.; Narayanaswamy, N.G.; Kurra, S.; Priyadarshini, A. A Portable Device for Single Point Strain Analysis in Sheet Metal Forming Processes. *HardwareX* **2022**, *12*, e00371. [CrossRef] [PubMed]
74. *ASTM E2218-14e1*; E28 Committee Test Method for Determining Forming Limit Curves. ASTM International: West Conshohocken, PA, USA, 2015.
75. Iadicola, M.A. Augmented Use of Standard Mechanical Testing Measurements for Sheet Metal Forming: Digital Image Correlation for Localized Necking. In *AIP Conference Proceedings*; American Institute of Physics: Melbourne, Australia, 2013; pp. 614–619.
76. Shi, B.-Q.; Liang, J. Circular Grid Pattern Based Surface Strain Measurement System for Sheet Metal Forming. *Opt. Lasers Eng.* **2012**, *50*, 1186–1195. [CrossRef]
77. Blaber, J.; Adair, B.; Antoniou, A. Ncorr: Open-Source 2D Digital Image Correlation Matlab Software. *Exp. Mech.* **2015**, *55*, 1105–1122. [CrossRef]
78. Yang, J.; Bhattacharya, K. Augmented Lagrangian Digital Image Correlation. *Exp. Mech.* **2019**, *59*, 187–205. [CrossRef]
79. Belloni, V.; Ravanelli, R.; Nascetti, A.; Di Rita, M.; Mattei, D.; Crespi, M. py2DIC: A New Free and Open Source Software for Displacement and Strain Measurements in the Field of Experimental Mechanics. *Sensors* **2019**, *19*, 3832. [CrossRef] [PubMed]
80. Olufsen, S.N.; Andersen, M.E.; Fagerholt, E. μ DIC: An Open-Source Toolkit for Digital Image Correlation. *SoftwareX* **2020**, *11*, 100391. [CrossRef]

81. Solav, D.; Moerman, K.M.; Jaeger, A.M.; Genovese, K.; Herr, H.M. MultiDIC: An Open-Source Toolbox for Multi-View 3D Digital Image Correlation. *IEEE Access* **2018**, *6*, 30520–30535. [CrossRef]
82. Farahnak, P.; Urbánek, M.; Konopík, P.; Džugan, J. Influence of Thickness Reduction on Forming Limits of Mild Steel DC01. *Int. J. Mater. Form.* **2020**, *13*, 371–381. [CrossRef]
83. Farahnak, P.; Urbanek, M.; Džugan, J. Investigation Study on Determination of Fracture Strain and Fracture Forming Limit Curve Using Different Experimental and Numerical Methods. *J. Phys. Conf. Ser.* **2017**, *896*, 012082. [CrossRef]
84. Min, J.; Stoughton, T.B.; Carsley, J.E.; Lin, J. Comparison of DIC Methods of Determining Forming Limit Strains. *Procedia Manuf.* **2017**, *7*, 668–674. [CrossRef]
85. Gkolfinopoulos, I.; Chijiwa, N. Determination of Johnson–Cook Material and Failure Model Constants for High-Tensile-Strength Tendon Steel in Post-Tensioned Concrete Members. *Appl. Sci.* **2022**, *12*, 7774. [CrossRef]
86. Jaremenko, C.; Huang, X.; Affronti, E.; Merklein, M.; Maier, A. Sheet Metal Forming Limits as Classification Problem. In Proceedings of the 2017 Fifteenth IAPR International Conference on Machine Vision Applications (MVA), Nagoya, Japan, 8–12 May 2017; IEEE: Nagoya, Japan, 2017; pp. 113–116.
87. Lu, Z.; Li, D.; Cao, L.; Cui, H.; Xu, J. Springback Control in Complex Sheet-Metal Forming Based on Advanced High-Strength Steel. *Coatings* **2023**, *13*, 930. [CrossRef]
88. Behrens, B.-A.; Rosenbusch, D.; Wester, H.; Dykiert, M. Comparison of Different Testing Approaches to Describe the Fracture Behaviour of AHSS Sheets Using Experimental and Numerical Investigations. *IOP Conf. Ser. Mater. Sci. Eng.* **2021**, *1157*, 012059. [CrossRef]
89. Saxena, K.; Drotleff, K.; Mukhopadhyay, J. Design of New Punch Geometries for Generation of Non-Linear Strain Paths and Formability Evaluation. *Light Metal Age*, 24 December 2015.
90. He, J.; Zeng, D.; Zhu, X.; Cedric Xia, Z.; Li, S. Effect of Nonlinear Strain Paths on Forming Limits under Isotropic and Anisotropic Hardening. *Int. J. Solids Struct.* **2014**, *51*, 402–415. [CrossRef]
91. Wi, M.S.; Lee, S.Y.; Barlat, F. Non-Linear Strain Path Experiment and Modeling for Very High Strength Material. *IOP Conf. Ser. Mater. Sci. Eng.* **2019**, *651*, 012005. [CrossRef]
92. Rocha, A.B.D.; Jalinier, J.M. Plastic Instability of Sheet Metals under Simple and Complex Strain Paths. *ISIJ Int.* **1984**, *24*, 132–140. [CrossRef]
93. Panich, S.; Chongbunwatana, K.; Kamonrattanapisud, M. Formability Prediction of Advanced High-Strength Steel Sheets by Means of Combined Experimental and Numerical Approaches. *Procedia Manuf.* **2019**, *29*, 528–535. [CrossRef]
94. Manopulo, N.; Hora, P.; Peters, P.; Gorji, M.; Barlat, F. An Extended Modified Maximum Force Criterion for the Prediction of Localized Necking under Non-Proportional Loading. *Int. J. Plast.* **2015**, *75*, 189–203. [CrossRef]
95. Volk, W.; Hoffmann, H.; Suh, J.; Kim, J. Failure Prediction for Nonlinear Strain Paths in Sheet Metal Forming. *CIRP Ann.* **2012**, *61*, 259–262. [CrossRef]
96. Chung, K.; Kim, H.; Lee, C. Forming Limit Criterion for Ductile Anisotropic Sheets as a Material Property and Its Deformation Path Insensitivity. Part I: Deformation Path Insensitive Formula Based on Theoretical Models. *Int. J. Plast.* **2014**, *58*, 3–34. [CrossRef]
97. Ma, L.; Wang, Z. The Effects of Through-Thickness Shear Stress on the Formability of Sheet Metal–A Review. *J. Manuf. Process.* **2021**, *71*, 269–289. [CrossRef]
98. Hickey, K. Shear Fracture. Available online: https://ahssinsights.org/forming/formability/shear-fracture/ (accessed on 5 June 2023).
99. Luo, M.; Chen, X.; Shi, M.F.; Shih, H.-C.; Barlat, F.; Moon, Y.H.; Lee, M.G. Numerical Analysis of AHSS Fracture in a Stretch-Bending Test. In *AIP Conference Proceedings*; American Institute of Physics: Pohang, Republic of Korea, 2010; pp. 455–463.
100. Huang, S.; Zhao, Y.; He, C. Stamping Failure Analysis of Advanced High Strength Steel Sheet Based on Non-Uniform Local Deformation through Thickness. In *AIP Conference Proceedings*; American Institute of Physics: Melbourne, Australia, 2013; pp. 583–586.
101. Li, Y.; Luo, M.; Gerlach, J.; Wierzbicki, T. Prediction of Shear-Induced Fracture in Sheet Metal Forming. *J. Mater. Process. Technol.* **2010**, *210*, 1858–1869. [CrossRef]
102. Wierzbicki, T.; Bao, Y.; Lee, Y.-W.; Bai, Y. Calibration and Evaluation of Seven Fracture Models. *Int. J. Mech. Sci.* **2005**, *47*, 719–743. [CrossRef]
103. Magrinho, J.P.; Silva, M.B.; Reis, L.; Martins, P.A.F. Formability Limits, Fractography and Fracture Toughness in Sheet Metal Forming. *Materials* **2019**, *12*, 1493. [CrossRef]
104. Magrinho, J.P.; Silva, M.B.; Martins, P.A.F. Experimental Determination of the Fracture Forming Limits in Metal Forming. *Discov. Mech. Eng.* **2023**, *2*, 7. [CrossRef]
105. Roth, C.C.; Mohr, D. Determining the Strain to Fracture for Simple Shear for a Wide Range of Sheet Metals. *Int. J. Mech. Sci.* **2018**, *149*, 224–240. [CrossRef]
106. Manopulo, D.N.; AutoForm. Advanced Formability Analysis: Moving Beyond the Limitations of the Traditional FLD for an Accurate and Streamlined Formability Analysis. FormingWorld. 2022. Available online: https://formingworld.com/advanced-formability-analysis-fld/ (accessed on 25 October 2023).
107. Nasheralahkami, S.; Zhou, W.; Golovashchenko, S. Study of Sheared Edge Formability of Ultra-High Strength DP980 Sheet Metal Blanks. *J. Manuf. Sci. Eng.* **2019**, *141*, 091009. [CrossRef]

108. Matsuno, T.; Mizumura, M.; Seto, A.; Suehiro, M. Improvement in Hole Expansion Ratio by Chamfered Die Edge. *J. JSTP* **2013**, *54*, 353–357. [CrossRef]
109. Shih, H.-C.; Hsiung, C.-K.; Wendt, B. Optimal Production Trimming Process for AHSS Sheared Edge Stretchability Improvement. *SAE Technical Paper*, 1 April 2014; pp. 2014–01–0994.
110. Frómeta, D.; Tedesco, M.; Calvo, J.; Lara, A.; Molas, S.; Casellas, D. Assessing Edge Cracking Resistance in AHSS Automotive Parts by the Essential Work of Fracture Methodology. *J. Phys. Conf. Ser.* **2017**, *896*, 012102. [CrossRef]
111. Feistle, M.; Kindsmüller, A.; Pätzold, I.; Golle, R.; Volk, W. Influence of Sheet Metal Pre-Forming on Edge Crack Sensitivity Using an AHSS Steel Grade. *Int. J. Mater. Form.* **2022**, *15*, 50. [CrossRef]
112. Neuhauser, F.M.; Terrazas, O.R.; Manopulo, N.; Hora, P.; Van Tyne, C.J. Stretch Bending—The Plane within the Sheet Where Strains Reach the Forming Limit Curve. *IOP Conf. Ser. Mater. Sci. Eng.* **2016**, *159*, 012011. [CrossRef]
113. Neuhauser, F.M.; Terrazas, O.; Manopulo, N.; Hora, P.; Van Tyne, C. The Bending Dependency of Forming Limit Diagrams. *Int. J. Mater. Form.* **2019**, *12*, 815–825. [CrossRef]
114. Levy, B.S.; Van Tyne, C.J. Predicting Breakage on a Die Radius with a Straight Bend Axis during Sheet Forming. *J. Mater. Process. Technol.* **2009**, *209*, 2038–2046. [CrossRef]
115. Kitting, D.; Ofenheimer, A.; Pauli, H.; Till, E.T. A Phenomenological Concept to Predict Formability in Stretch-Bending Forming Operations. *Int. J. Mater. Form.* **2010**, *3*, 1163–1166. [CrossRef]
116. Kitting, D.; Ofenheimer, A.; Pauli, H.; Till, E.T. Experimental Characterization of Stretch-Bending Formability of AHSS Sheets. In *AIP Conference Proceedings*; American Institute of Physics: Belfast, UK, 2011; pp. 1589–1594.
117. Borrego, M.; Morales-Palma, D.; Martínez-Donaire, A.J.; Centeno, G.; Vallellano, C. Analysis of Formability in Conventional Hole Flanging of AA7075-O Sheets: Punch Edge Radius Effect and Limitations of the FLC. *Int. J. Mater. Form.* **2020**, *13*, 303–316. [CrossRef]
118. Jadhav, S.; Schoiswohl, M.; Buchmayr, B. Applications of Finite Element Simulation in the Development of Advanced Sheet Metal Forming Processes. *Berg Huettenmaenn. Monatsh.* **2018**, *163*, 109–118. [CrossRef]
119. Chen, K.; Lin, J.P. Material Modeling and Correlative Mechanical Testing on AHSS Sheet Forming Simulation. *AMR* **2011**, *337*, 198–202. [CrossRef]
120. Banabic, D. Yield Criteria for Isotropic Materials. In *Sheet Metal Forming Processes*; Springer: Berlin/Heidelberg, Germany, 2010; ISBN 978-3-540-88112-4.
121. Tresca, H. On the Yield of Solids at High Pressures. *Comptes Rendus Acad. Des Sci.* **1864**, *59*, 754.
122. Huber, M. Przyczynek Do Podstaw Wytorymalosci. *Czasop. Tech.* **1904**, *22*, 81.
123. Hencky, H. Zur Theorie plastischer Deformationen und der hierdurch im Material hervorgerufenen Nachspannungen. *Z. Angew. Math. Mech.* **1924**, *4*, 323–334. [CrossRef]
124. Mises, R. Mechanics of Solids in Plastic State (Almanca), Göttinger Nachrichten Math. *Phys. Kl.* **1913**, *4*, 582–592.
125. Drucker, D.C. Relation of Experiments to Mathematical Theories of Plasticity. *J. Appl. Mech.* **1949**, *16*, 349–357. [CrossRef]
126. Hershey, A.V. The Plasticity of an Isotropic Aggregate of Anisotropic Face-Centered Cubic Crystals. *J. Appl. Mech.* **1954**, *21*, 241–249. [CrossRef]
127. Hill, R. A Theory of the Yielding and Plastic Flow of Anisotropic Metals. *Proc. R. Soc. Lond. A* **1948**, *193*, 281–297. [CrossRef]
128. Hill, R. Theoretical Plasticity of Textured Aggregates. *Math. Proc. Camb. Phil. Soc.* **1979**, *85*, 179–191. [CrossRef]
129. Barlat, F.; Brem, J.C.; Yoon, J.W.; Chung, K.; Dick, R.E.; Lege, D.J.; Pourboghrat, F.; Choi, S.-H.; Chu, E. Plane Stress Yield Function for Aluminum Alloy Sheets—Part 1: Theory. *Int. J. Plast.* **2003**, *19*, 1297–1319. [CrossRef]
130. Aretz, H. General Orthotropic Yield Functions Based on Linear Stress Deviator Transformations. In *AIP Conference Proceedings*; AIP: Columbus, OH, USA, 2004; Volume 712, pp. 147–156.
131. Barlat, F.; Brem, J.; Yoon, J.; Dick, R.; Choi, S.; Chung, K.; Lege, D. Constitutive Modeling for Aluminium Sheet Forming Simulations. In Proceedings of the 8th International Symposium on Plasticity and Its Current Applications, Whistler, CA, USA, 16–20 July 2000; pp. 591–593.
132. Barlat, F.; Aretz, H.; Yoon, J.W.; Karabin, M.E.; Brem, J.C.; Dick, R.E. Linear Transfomation-Based Anisotropic Yield Functions. *Int. J. Plast.* **2005**, *21*, 1009–1039. [CrossRef]
133. Banabic, D. An Improved Analytical Description of Orthotropy in Metallic Sheets. *Int. J. Plast.* **2005**, *21*, 493–512. [CrossRef]
134. Banabic, D. Yield Criterion for Orthotropic Sheet Metals. In Proceedings of the 8th International Conference on Metal Forming, Krakow, Poland, 3–7 September 2000; pp. 755–761.
135. Cazacu, O.; Barlat, F. Generalization of Drucker's Yield Criterion to Orthotropy. *Math. Mech. Solids* **2001**, *6*, 613–630. [CrossRef]
136. Abspoel, M.; Scholting, M.E.; Lansbergen, M.; An, Y.; Vegter, H. A New Method for Predicting Advanced Yield Criteria Input Parameters from Mechanical Properties. *J. Mater. Process. Technol.* **2017**, *248*, 161–177. [CrossRef]
137. Vegter, H.; Van Den Boogaard, A.H. A Plane Stress Yield Function for Anisotropic Sheet Material by Interpolation of Biaxial Stress States. *Int. J. Plast.* **2006**, *22*, 557–580. [CrossRef]
138. Ludwik, P. *Elemente Der Technologischen Mechanik*; Springer: Berlin/Heidelberg, Germany, 1909; ISBN 3-662-39265-8.
139. Swift, H.W. Plastic Instability under Plane Stress. *J. Mech. Phys. Solids* **1952**, *1*, 1–18. [CrossRef]
140. Voce, E. The Relationship between Stress and Strain for Homogeneous Deformation. *J. Inst. Met.* **1948**, *74*, 537–562.
141. Prager, W. A New Method of Analyzing Stresses and Strains in Work-Hardening Plastic Solids. *J. Appl. Mech.* **1956**, *23*, 493–496. [CrossRef]

142. Armstrong, P.J.; Frederick, C. *A Mathematical Representation of the Multiaxial Bauschinger Effect*; Berkeley Nuclear Laboratories: Berkeley, CA, USA, 1966; Volume 731.
143. Chaboche, J.L. Time-Independent Constitutive Theories for Cyclic Plasticity. *Int. J. Plast.* **1986**, *2*, 149–188. [CrossRef]
144. Yoshida, F.; Uemori, T. A Model of Large-Strain Cyclic Plasticity Describing the Bauschinger Effect and Workhardening Stagnation. *Int. J. Plast.* **2002**, *18*, 661–686. [CrossRef]
145. CIRP—The International Academy for Production Engineering; Laperrière, L. (Eds.) *CIRP Encyclopedia of Production Engineering. Volume 1: A-H*, 2nd ed.; Springer: Berlin/Heidelberg, Germany, 2019; ISBN 978-3-662-53120-4.
146. Yoshida, F.; Hamasaki, H.; Uemori, T. A User-Friendly 3D Yield Function to Describe Anisotropy of Steel Sheets. *Int. J. Plast.* **2013**, *45*, 119–139. [CrossRef]
147. Eriksson, A. Non-Linear Strain Paths in Sheet Metal Forming. Master's Thesis, Blekinge Institute of Technology, Karlskrona, Sweden, 2021.
148. Güner, D.A.; Technical Product Manager AutoForm. Material Matters: Sheet Metal Plasticity Visualized (Part 1 of 2). FormingWorld. 2016. Available online: https://formingworld.com/sheet-metal-plasticity-visualized-part-1-of-2/ (accessed on 25 October 2023).
149. Mu, Z.; Zhao, J.; Meng, Q.; Zhang, Y.; Yu, G. Limitation Analysis of the Hill48 Yield Model and Establishment of Its Modified Model for Planar Plastic Anisotropy. *J. Mater. Process. Technol.* **2022**, *299*, 117380. [CrossRef]
150. Gutierrez, J.E.; Noder, J.; Butcher, C. Experimental Characterization and Deterministic Prediction of In-Plane Formability of 3rd Generation Advanced High Strength Steels. *Metals* **2020**, *10*, 902. [CrossRef]
151. Gösling, M. Influence of Yield Condition on the Accuracy of Earing Prediction for Steel Sheets. *J. Phys. Conf. Ser.* **2016**, *734*, 032045. [CrossRef]
152. Cai, Z.; Diao, K.; Wu, X.; Wan, M. Constitutive Modeling of Evolving Plasticity in High Strength Steel Sheets. *Int. J. Mech. Sci.* **2016**, *107*, 43–57. [CrossRef]
153. Cheng, C.; Wan, M.; Wu, X.D.; Cai, Z.Y.; Zhao, R.; Meng, B. Effect of Yield Criteria on the Formability Prediction of Dual-Phase Steel Sheets. *Int. J. Mech. Sci.* **2017**, *133*, 28–41. [CrossRef]
154. Panich, S.; Barlat, F.; Uthaisangsuk, V.; Suranuntchai, S.; Jirathearanat, S. Experimental and Theoretical Formability Analysis Using Strain and Stress Based Forming Limit Diagram for Advanced High Strength Steels. *Mater. Des.* **2013**, *51*, 756–766. [CrossRef]
155. Li, Q.-M.; Yi, Z.-W.; Liu, Y.-Q.; Tang, X.-F.; Jiang, W.; Li, H.-J. Explicit Analysis of Sheet Metal Forming Processes Using Solid-Shell Elements. *Metals* **2021**, *12*, 52. [CrossRef]
156. Britez, D.; Werda, S.; Laheurte, R.; Darnis, P.; Cahuc, O. A comparison of different hardening rules on a multi-step global manufacturing process modeling. In Proceedings of the 24th International Conference on Material Forming ESAFORM 2021, Liège, Belgium, 14–16 April 2021. [CrossRef]
157. Feigenbaum, H.P.; Dafalias, Y.F. Directional Distortional Hardening in Metal Plasticity within Thermodynamics. *Int. J. Solids Struct.* **2007**, *44*, 7526–7542. [CrossRef]
158. Zhu, H.; Lin, Y.; Chen, K.; He, Z.; Yuan, S. A Homogeneous Anisotropic Hardening Model in Plane Stress State for Sheet Metal under Nonlinear Loading Paths. *Materials* **2023**, *16*, 1151. [CrossRef]
159. Cyclic Hardening. Available online: https://2021.help.altair.com/2021.0.1/form/en_us/topics/form/reference/cyclic_hardening_r.htm (accessed on 8 June 2023).
160. Stoughton, T.B.; Yoon, J.W. Anisotropic Hardening and Non-Associated Flow in Proportional Loading of Sheet Metals. *Int. J. Plast.* **2009**, *25*, 1777–1817. [CrossRef]
161. Chen, Z.; Wang, Y.; Lou, Y. User-Friendly Anisotropic Hardening Function with Non-Associated Flow Rule under the Proportional Loadings for BCC and FCC Metals. *Mech. Mater.* **2022**, *165*, 104190. [CrossRef]
162. Rosenschon, M.; Merklein, M. Analysis of the Stress and Directional Dependent Bauschinger-Effect of Sheet Metals. *IOP Conf. Ser. Mater. Sci. Eng.* **2018**, *418*, 012084. [CrossRef]
163. Rokhgireh, H.; Nayebi, A.; Chaboche, J.L. Application of a New Distortional Yield Surface Model in Cyclic Uniaxial and Multiaxial Loading. *Int. J. Solids Struct.* **2017**, *110*, 219–238. [CrossRef]
164. Qin, J.; Holmedal, B.; Hopperstad, O.S. A Combined Isotropic, Kinematic and Distortional Hardening Model for Aluminum and Steels under Complex Strain-Path Changes. *Int. J. Plast.* **2018**, *101*, 156–169. [CrossRef]
165. Holmedal, B. Bauschinger Effect Modelled by Yield Surface Distortions. *Int. J. Plast.* **2019**, *123*, 86–100. [CrossRef]
166. Yang, H.; Zhang, W.; Zhuang, X.; Zhao, Z. Phenomenological Modeling of Deformation-Induced Anisotropic Hardening Behaviors: A Review. *Metals* **2023**, *13*, 364. [CrossRef]
167. Butuc, M.C.; Teodosiu, C.; Barlat, F.; Gracio, J.J. Analysis of Sheet Metal Formability through Isotropic and Kinematic Hardening Models. *Eur. J. Mech.-A/Solids* **2011**, *30*, 532–546. [CrossRef]
168. Abbasnejad Dizaji, S.; Darendeliler, H.; Kaftanoğlu, B. Effect of Hardening Models on Different Ductile Fracture Criteria in Sheet Metal Forming. *Int. J. Mater. Form.* **2016**, *9*, 261–267. [CrossRef]
169. Lemaitre, J.; Chaboche, J.-L. *Mechanics of Solid Materials*, 1st ed.; Cambridge University Press: Cambridge, UK, 1990; ISBN 978-0-521-32853-1.
170. Brozzo, P.; Deluca, B.; Rendina, R. A New Method for the Prediction of Formability Limits of Metal Sheets. In Proceedings of the 7th Biennial Conference, Amsterdam, The Netherlands, 9–13 October 1972.
171. Cockcroft, M. Ductility and Workability of Metals. *J. Met.* **1968**, *96*, 2444.

172. Ayada, M. Central Bursting in Extrusion of Inhomogeneous Materials. In Proceedings of the 2nd International Conference on Technology for Plasticity, Stuttgart, Germany, 24–28 August 1987; pp. 553–558.
173. Stoughton, T.B. A Non-Associated Flow Rule for Sheet Metal Forming. *Int. J. Plast.* **2002**, *18*, 687–714. [CrossRef]
174. Min, J.; Carsley, J.E.; Lin, J.; Wen, Y.; Kuhlenkötter, B. A Non-Quadratic Constitutive Model under Non-Associated Flow Rule of Sheet Metals with Anisotropic Hardening: Modeling and Experimental Validation. *Int. J. Mech. Sci.* **2016**, *119*, 343–359. [CrossRef]
175. Lee, E.-H.; Stoughton, T.B.; Yoon, J.W. A Yield Criterion through Coupling of Quadratic and Non-Quadratic Functions for Anisotropic Hardening with Non-Associated Flow Rule. *Int. J. Plast.* **2017**, *99*, 120–143. [CrossRef]
176. Park, N.; Stoughton, T.B.; Yoon, J.W. A Criterion for General Description of Anisotropic Hardening Considering Strength Differential Effect with Non-Associated Flow Rule. *Int. J. Plast.* **2019**, *121*, 76–100. [CrossRef]
177. Hou, Y.; Du, K.; El-Aty, A.A.; Lee, M.-G.; Min, J. Plastic Anisotropy of Sheet Metals under Plane Strain Loading: A Novel Non-Associated Constitutive Model Based on Fourth-Order Polynomial Functions. *Mater. Des.* **2022**, *223*, 111187. [CrossRef]
178. Lou, Y.; Zhang, C.; Zhang, S.; Yoon, J.W. A General Yield Function with Differential and Anisotropic Hardening for Strength Modelling under Various Stress States with Non-Associated Flow Rule. *Int. J. Plast.* **2022**, *158*, 103414. [CrossRef]
179. Lian, J.; Sharaf, M.; Archie, F.; Münstermann, S. A Hybrid Approach for Modelling of Plasticity and Failure Behaviour of Advanced High-Strength Steel Sheets. *Int. J. Damage Mech.* **2013**, *22*, 188–218. [CrossRef]
180. Fu, Q.T.; Li, D.; Song, H.; Liu, X.F.; Xu, J.C.; Jiang, N. Shear Fracture Criterion of Advanced High-Strength Steel Based on Stress Triaxiality and Equivalent Strain. *J. Eng. Mater. Technol.* **2023**, *145*, 011002. [CrossRef]
181. Rossi, M.; Lattanzi, A.; Morichelli, L.; Martins, J.M.P.; Thuillier, S.; Andrade-Campos, A.; Coppieters, S. Testing Methodologies for the Calibration of Advanced Plasticity Models for Sheet Metals: A Review. *Strain* **2022**, *58*, e12426. [CrossRef]
182. Chica, J.C.; Bravo Díez, P.M.; Preciado Calzada, M. Improved Correlation for Elastic Modulus Prediction of Metallic Materials in the Small Punch Test. *Int. J. Mech. Sci.* **2017**, *134*, 112–122. [CrossRef]
183. Roth, C.C.; Mohr, D. Ductile Fracture Experiments with Locally Proportional Loading Histories. *Int. J. Plast.* **2016**, *79*, 328–354. [CrossRef]
184. Miyauchi, M. A Proposal of a Planar Simple Shear Test in Sheet Metals. *Sci. Pap. Inst. Phys. Chem. Res.* **1984**, *78*, 27–40.
185. Bouvier, S.; Haddadi, H.; Levée, P.; Teodosiu, C. Simple Shear Tests: Experimental Techniques and Characterization of the Plastic Anisotropy of Rolled Sheets at Large Strains. *J. Mater. Process. Technol.* **2006**, *172*, 96–103. [CrossRef]
186. Rauch, E.F.; G'Sell, C. Flow Localization Induced by a Change in Strain Path in Mild Steel. *Mater. Sci. Eng. A* **1989**, *111*, 71–80. [CrossRef]
187. Genevois, P. Etude Expérimental et Modélisation Du Comportement Plastique Anisotrope de Tôles d'acier En Grandes Déformations. Ph.D. Thesis, Institut National Polytechnique de Grenoble, Grenoble, France, 1992.
188. *ASTM B831-93*; B07 Committee Test Method for Shear Testing of Thin Aluminum Alloy Products. ASTM International: West Conshohocken, PA, USA, 2023.
189. Beese, A.M.; Mohr, D. Effect of Stress Triaxiality and Lode Angle on the Kinetics of Strain-Induced Austenite-to-Martensite Transformation. *Acta Mater.* **2011**, *59*, 2589–2600. [CrossRef]
190. Yin, Q.; Soyarslan, C.; Isik, K.; Tekkaya, A.E. A Grooved In-Plane Torsion Test for the Investigation of Shear Fracture in Sheet Materials. *Int. J. Solids Struct.* **2015**, *66*, 121–132. [CrossRef]
191. Iosipescu, N. New Accurate Procedure for Single Shear Testing of Metals. *J. Mater.* **1967**, *2*, 537–566.
192. *ASTM D5379/D5379M-19*; D30 Committee Test Method for Shear Properties of Composite Materials by the V-Notched Beam Method. ASTM International: West Conshohocken, PA, USA, 2019.
193. Bao, Y.; Wierzbicki, T. On Fracture Locus in the Equivalent Strain and Stress Triaxiality Space. *Int. J. Mech. Sci.* **2004**, *46*, 81–98. [CrossRef]
194. Shouler, D.R.; Allwood, J.M. Design and Use of a Novel Sample Design for Formability Testing in Pure Shear. *J. Mater. Process. Technol.* **2010**, *210*, 1304–1313. [CrossRef]
195. Dunand, M.; Mohr, D. Optimized Butterfly Specimen for the Fracture Testing of Sheet Materials under Combined Normal and Shear Loading. *Eng. Fract. Mech.* **2011**, *78*, 2919–2934. [CrossRef]
196. Khameneh, F.; Abedini, A.; Butcher, C. Experimental and Numerical Fracture Characterization of DP1180 Steel in Combined Simple Shear and Uniaxial Tension. *Metals* **2023**, *13*, 1305. [CrossRef]
197. Peirs, J.; Verleysen, P.; Degrieck, J. Novel Technique for Static and Dynamic Shear Testing of Ti6Al4V Sheet. *Exp. Mech.* **2012**, *52*, 729–741. [CrossRef]
198. Brosius, A.; Yin, Q.; Güner, A.; Tekkaya, A.E. A New Shear Test for Sheet Metal Characterization. *Steel Res. Int.* **2011**, *82*, 323–328. [CrossRef]
199. Yin, Q.; Tekkaya, A.E.; Traphöner, H. Determining Cyclic Flow Curves Using the In-Plane Torsion Test. *CIRP Ann.* **2015**, *64*, 261–264. [CrossRef]
200. Grolleau, V.; Roth, C.C.; Mohr, D. Characterizing Plasticity and Fracture of Sheet Metal through a Novel In-Plane Torsion Experiment. *IOP Conf. Ser. Mater. Sci. Eng.* **2019**, *651*, 012101. [CrossRef]
201. *ASTM E8-00b*; E28 Committee Test Methods for Tension Testing of Metallic Materials. ASTM International: West Conshohocken, PA, USA, 2001.
202. Marcadet, S.J.; Mohr, D. Effect of Compression–Tension Loading Reversal on the Strain to Fracture of Dual Phase Steel Sheets. *Int. J. Plast.* **2015**, *72*, 21–43. [CrossRef]

203. Peng, J.; Zhou, P.; Wang, Y.; Dai, Q.; Knowles, D.; Mostafavi, M. Stress Triaxiality and Lode Angle Parameter Characterization of Flat Metal Specimen with Inclined Notch. *Metals* **2021**, *11*, 1627. [CrossRef]
204. Bai, Y.; Wierzbicki, T. Application of Extended Mohr–Coulomb Criterion to Ductile Fracture. *Int. J. Fract.* **2010**, *161*, 1–20. [CrossRef]
205. Jia, Y.; Bai, Y. Ductile Fracture Prediction for Metal Sheets Using All-Strain-Based Anisotropic eMMC Model. *Int. J. Mech. Sci.* **2016**, *115*, 516–531. [CrossRef]
206. Santos, R.O.; Moreira, L.P.; Butuc, M.C.; Vincze, G.; Pereira, A.B. Damage Analysis of Third-Generation Advanced High-Strength Steel Based on the Gurson–Tvergaard–Needleman (GTN) Model. *Metals* **2022**, *12*, 214. [CrossRef]
207. *ISO 16808: 2014*; Metallic Materials—Sheet and Strip—Determination of Biaxial Stress–Strain Curve by Means of Bulge Test with Optical Measuring Systems. ISO: Geneva, Switzerland, 2014.
208. Lancaster, R.J.; Jeffs, S.P.; Haigh, B.J.; Barnard, N.C. Derivation of Material Properties Using Small Punch and Shear Punch Test Methods. *Mater. Des.* **2022**, *215*, 110473. [CrossRef]
209. *ASTM E3205-20*; E10 Committee Standard Test Method for Small Punch Testing of Metallic Materials. ASTM International: West Conshohocken, PA, USA, 2020.
210. Mohr, D.; Henn, S. Calibration of Stress-Triaxiality Dependent Crack Formation Criteria: A New Hybrid Experimental–Numerical Method. *Exp. Mech.* **2007**, *47*, 805–820. [CrossRef]
211. Bai, Y. Effect of Loading History in Necking and Fracture. Ph.D. Thesis, Massachusetts Institute of Technology, Cambridge, MA, USA, 2008.
212. Peshekhodov, I.; Jiang, S.; Vucetic, M.; Bouguecha, A.; Berhens, B.-A. Experimental-Numerical Evaluation of a New Butterfly Specimen for Fracture Characterisation of AHSS in a Wide Range of Stress States. *IOP Conf. Ser. Mater. Sci. Eng.* **2016**, *159*, 012015. [CrossRef]
213. Behrens, B.A.; Dykiert, M.; Wester, H.; Stockburger, E.; Jegatheeswaran, V. Improved Failure Characterisation of High-Strength Steel Using a Butterfly Test Rig with Rotation Control. *Mater. Res. Proc.* **2023**, *28*, 737–746.
214. Aisvaran, C. Study of Non-Linear Strain Path in Sheet Metal Forming. Master's Thesis, Faculty of Engineering, Blekinge Institute of Technology, Karlskrona, Sweden, 2021.
215. Gaber, C.; Jocham, D.; Weiss, H.A.; Böttcher, O.; Volk, W. Evaluation of Non-Linear Strain Paths Using Generalized Forming Limit Concept and a Modification of the Time Dependent Evaluation Method. *Int. J. Mater. Form.* **2017**, *10*, 345–351. [CrossRef]
216. Song, X.; Leotoing, L.; Guines, D.; Ragneau, E. Identification of Forming Limits at Fracture of DP600 Sheet Metal under Linear and Unloaded Non-Linear Strain Paths. *Procedia Eng.* **2017**, *207*, 562–567. [CrossRef]
217. Song, X.; Leotoing, L.; Guines, D.; Ragneau, E. Effect of Continuous Strain Path Changes on Forming Limit Strains of DP600. *Strain* **2019**, *55*, e12329. [CrossRef]
218. Saxena, K.; Kumar, D.; Mukhopadhyay, J. A Novel Experimental Approach for Detection of Forming Limits Considering Non Linear Strain Paths. In International Deep Drawing Research Group (IDDRG) Conference. Shanghai, China, 31 May–3 June 2015; pp. 244–261.
219. Drotleff, K.; Panich, S.; Liewald, M.; Uthaisangsuk, V. Experimental and numerical formability analysis of advanced high strength steel for deep drawing using the nonlinear strain path forming limit. In Proceedings of the Forming Technology Forum 2016, San Diego, CA, USA, 18–19 October 2016.
220. Jocham, D.; Gaber, C.; Böttcher, O.; Volk, W. Prediction of Formability for Multi-Linear Strain Paths. In Proceedings of the Forming Technology Forum 2015, Glasgow, UK, 29 June 2015.
221. He, Z.; Zhu, H.; Lin, Y.; Politis, D.J.; Wang, L.; Yuan, S. A Novel Test Method for Continuous Nonlinear Biaxial Tensile Deformation of Sheet Metals by Bulging with Stepped-Dies. *Int. J. Mech. Sci.* **2020**, *169*, 105321. [CrossRef]
222. Pack, K.; Mohr, D. Combined Necking & Fracture Model to Predict Ductile Failure with Shell Finite Elements. *Eng. Fract. Mech.* **2017**, *182*, 32–51. [CrossRef]
223. Pack, K.; Tancogne-Dejean, T.; Gorji, M.B.; Mohr, D. Hosford-Coulomb Ductile Failure Model for Shell Elements: Experimental Identification and Validation for DP980 Steel and Aluminum 6016-T4. *Int. J. Solids Struct.* **2018**, *151*, 214–232. [CrossRef]
224. Wang, S.; Wang, Y.; Yu, L.; Ji, K.; Liu, X.; Lou, Y. Failure Modeling for QP980 Steel by a Shear Ductile Fracture Criterion. *Metals* **2022**, *12*, 452. [CrossRef]
225. Cherouat, A.; Borouchaki, H.; Jie, Z. Simulation of Sheet Metal Forming Processes Using a Fully Rheological-Damage Constitutive Model Coupling and a Specific 3D Remeshing Method. *Metals* **2018**, *8*, 991. [CrossRef]
226. Erice, B.; Roth, C.C.; Mohr, D. Stress-State and Strain-Rate Dependent Ductile Fracture of Dual and Complex Phase Steel. *Mech. Mater.* **2018**, *116*, 11–32. [CrossRef]
227. Sandin, O.; Jonsén, P.; Frómeta, D.; Casellas, D. Stating Failure Modelling Limitations of High Strength Sheets: Implications to Sheet Metal Forming. *Materials* **2021**, *14*, 7821. [CrossRef]
228. Luo, M.; Wierzbicki, T. Numerical Failure Analysis of a Stretch-Bending Test on Dual-Phase Steel Sheets Using a Phenomenological Fracture Model. *Int. J. Solids Struct.* **2010**, *47*, 3084–3102. [CrossRef]
229. Dunand, M.; Mohr, D. Ductile Fracture of AHSS Sheets under Multi-Axial Loading: Experiments and Modeling. In *AIP Conference Proceedings*; American Institute of Physics: Seoul, Republic of Korea, 2011; pp. 484–491.
230. Doig, M.; Roll, K. Assessment of Damage Models in Sheet Metal Forming for Industrial Applications. *KEM* **2011**, *473*, 482–489. [CrossRef]

231. Isik, K.; Soyarslan, C.; Richter, H.; Tekkaya, A.E. Analysis of Formability of Advanced High Strength Steel Sheets with Phenomenologically Based Failure Criteria with Separate Treatment of Instability, Shear and Normal Fracture. In Proceedings of the 8th European LS-DYNA Users Conference, Strasbourg, France, 23–24 May 2011.
232. Roth, C.C.; Mohr, D. Effect of Strain Rate on Ductile Fracture Initiation in Advanced High Strength Steel Sheets: Experiments and Modeling. *Int. J. Plast.* **2014**, *56*, 19–44. [CrossRef]
233. Mohr, D.; Marcadet, S.J. Micromechanically-Motivated Phenomenological Hosford–Coulomb Model for Predicting Ductile Fracture Initiation at Low Stress Triaxialities. *Int. J. Solids Struct.* **2015**, *67*, 40–55. [CrossRef]
234. Andrade, F.X.C.; Feucht, M.; Haufe, A.; Neukamm, F. An Incremental Stress State Dependent Damage Model for Ductile Failure Prediction. *Int. J. Fract.* **2016**, *200*, 127–150. [CrossRef]
235. Jia, Y.; Qiao, Y.; Pan, H.; Chu, E.; Bai, Y. A Comprehensive Plasticity and Fracture Model for Metal Sheets under Multi-Axial Stress and Non-Linear Strain Path. *SAE Int. J. Engines* **2017**, *10*, 266–273. [CrossRef]
236. Behrens, B.-A.; Bonk, C.; Peshekhodov, I. On Modelling of Shear Fracture in Deep Drawing of a High-Strength Dual-Phase Sheet Steel. *J. Phys. Conf. Ser.* **2017**, *896*, 012125. [CrossRef]
237. Heibel, S.; Nester, W.; Clausmeyer, T.; Tekkaya, A.E. Failure Assessment in Sheet Metal Forming Using a Phenomenological Damage Model and Fracture Criterion: Experiments, Parameter Identification and Validation. *Procedia Eng.* **2017**, *207*, 2066–2071. [CrossRef]
238. Chen, X.; Chen, G.; Huang, L. Validation of GISSMO Model for Fracture Prediction of a Third-Generation Advanced High-Strength Steel. *SAE Int. J. Mater. Manf.* **2018**, *11*, 293–302. [CrossRef]
239. Cui, X.-L.; Zhang, W.W.; Zhang, Z.-C.; Chen, Y.-Z.; Lin, P.; Chi, C.-Z. Prediction of Forming Limit of Dual-Phase 500 Steel Sheets Using the GTN Ductile Damage Model in an Innovative Hydraulic Bulging Test. *JOM* **2018**, *70*, 1542–1547. [CrossRef]
240. Achineethongkham, K.; Uthaisangsuk, V. Analysis of Forming Limit Behaviour of High Strength Steels under Non-Linear Strain Paths Using a Micromechanics Damage Modelling. *Int. J. Mech. Sci.* **2020**, *183*, 105828. [CrossRef]
241. Urbánek, M.; Fedorko, M.; Rund, M. Determination of Fracture Limit Line in Principal Strain Space by Shear Tests. *IOP Conf. Ser. Mater. Sci. Eng.* **2021**, *1178*, 012060. [CrossRef]
242. Fu, Q.; Li, D.; Song, H.; Liu, X.; Lu, Z.; Cui, H. Research on Parameters of MMC Fracture Criterion for Advanced High Strength Dual-Phase Steel Sheets. *J. Theor. Appl. Mech.* **2022**, *60*, 253–264. [CrossRef] [PubMed]
243. Prasad, K.; Gupta, A.; Krishnaswamy, H.; Chakkingal, U.; Banerjee, D.K.; Lee, M.-G. Does Friction Contribute to Formability Improvement Using Servo Press? *Friction* **2023**, *11*, 820–835. [CrossRef]
244. Cao, T.S. Models for Ductile Damage and Fracture Prediction in Cold Bulk Metal Forming Processes: A Review. *Int. J. Mater. Form.* **2017**, *10*, 139–171. [CrossRef]
245. Bai, Y.; Wierzbicki, T. A New Model of Metal Plasticity and Fracture with Pressure and Lode Dependence. *Int. J. Plast.* **2008**, *24*, 1071–1096. [CrossRef]
246. McClintock, F. Ductile Failure. *J. Appl. Mech.* **1968**, *35*, 363. [CrossRef]
247. Rice, J.R.; Tracey, D.M. On the Ductile Enlargement of Voids in Triaxial Stress Fields∗. *J. Mech. Phys. Solids* **1969**, *17*, 201–217. [CrossRef]
248. Oyane, M.; Sato, T.; Okimoto, K.; Shima, S. Criteria for Ductile Fracture and Their Applications. *J. Mech. Work. Technol.* **1980**, *4*, 65–81. [CrossRef]
249. Bao, Y.; Wierzbicki, T. A Comparative Study on Various Ductile Crack Formation Criteria. *J. Eng. Mater. Technol.* **2004**, *126*, 314–324. [CrossRef]
250. Kachanov, L. Time of the Rupture Process under Creep Condition. *TVZ Akad. Nauk. SSR Otd. Tech. Nauk* **1958**, *8*, 26–31.
251. Chaboche, J.-L. Anisotropic Creep Damage in the Framework of Continuum Damage Mechanics. *Nucl. Eng. Des.* **1984**, *79*, 309–319. [CrossRef]
252. Lemaitre, J. Local Approach of Fracture. *Eng. Fract. Mech.* **1986**, *25*, 523–537. [CrossRef]
253. Lemaitre, J.; Desmorat, R. *Engineering Damage Mechanics: Ductile, Creep, Fatigue and Brittle Failures*; Springer Science & Business Media: Berlin, Germany, 2006; ISBN 3-540-27293-3.
254. Cao, T.-S.; Gachet, J.-M.; Montmitonnet, P.; Bouchard, P.-O. A Lode-Dependent Enhanced Lemaitre Model for Ductile Fracture Prediction at Low Stress Triaxiality. *Eng. Fract. Mech.* **2014**, *124*, 80–96. [CrossRef]
255. Neukamm, F.; Feucht, M.; Roll, K.; Haufe, A. On Closing the Constitutive Gap between Forming and Crash Simulation. In Proceedings of the 10th International LS-DYNA Users Conference, Dearborn, MI, USA, 8 May 2008.
256. Basaran, M.; Weichert, D.; Wölkerling, S.D.; Feucht, M.; Neukamm, F. An Extension of the GISSMO Damage Model Based on Lode Angle Dependence. *LS-DYNA Anwenderforum* **2010**, *15*, 15.
257. Gurson, A.L. Continuum Theory of Ductile Rupture by Void Nucleation and Growth: Part I—Yield Criteria and Flow Rules for Porous Ductile Media. *J. Eng. Mater. Technol.* **1977**, *99*, 2–15. [CrossRef]
258. Tvergaard, V.; Needleman, A. Analysis of the Cup-Cone Fracture in a Round Tensile Bar. *Acta Metall.* **1984**, *32*, 157–169. [CrossRef]
259. Xue, L. Constitutive Modeling of Void Shearing Effect in Ductile Fracture of Porous Materials. *Eng. Fract. Mech.* **2008**, *75*, 3343–3366. [CrossRef]
260. Nahshon, K.; Hutchinson, J. Modification of the Gurson Model for Shear Failure. *Eur. J. Mech.-A/Solids* **2008**, *27*, 1–17. [CrossRef]

261. Uthaisangsuk, V.; Prahl, U.; Bleck, W. Characterisation of Formability Behaviour of Multiphase Steels by Micromechanical Modelling. *Int. J. Fract.* **2009**, *157*, 55–69. [CrossRef]
262. Zhang, Z. A Complete Gurson Model. In *Nonlinear Fracture and Damage Mechanics*; WIT Press: Southampton, UK, 2001.

Disclaimer/Publisher's Note: The statements, opinions and data contained in all publications are solely those of the individual author(s) and contributor(s) and not of MDPI and/or the editor(s). MDPI and/or the editor(s) disclaim responsibility for any injury to people or property resulting from any ideas, methods, instructions or products referred to in the content.